Neuroscience

An Anatomical and Physiological Basis for Flexible Coincidence Detection in the Auditory System

Reviewed Preprint
v1 • September 11, 2024
Not revised

Lauren J Kreeger, Suraj Honnuraiah, Sydney Maeker, Siobhan Shea, Gord Fishell, Lisa V Goodrich

Harvard Medical School, Department of Neurobiology, Boston, MA 02115, USA • Stanley Center for Psychiatric Research, Broad Institute of MIT and Harvard, Cambridge, MA 02142, USA

Abstract

Animals navigate the auditory world by recognizing complex sounds, from the rustle of a predator to the call of a potential mate. This ability depends in part on the octopus cells of the auditory brainstem, which respond to multiple frequencies that change over time, as occurs in natural stimuli. Unlike the average neuron, which integrates inputs over time on the order of tens of milliseconds, octopus cells must detect momentary coincidence of excitatory inputs from the cochlea during an ongoing sound on both the millisecond and submillisecond time scale. Here, we show that octopus cells receive inhibitory inputs on their dendrites that enhance opportunities for coincidence detection in the cell body, thereby allowing for responses both to rapid onsets at the beginning of a sound and to frequency modulations during the sound. This mechanism is crucial for the fundamental process of integrating the synchronized frequencies of natural auditory signals over time.

eLife assessment

This **valuable** work analyzes how specialized cells in the auditory cells, known as the octopus cells, can detect coincidences in their inputs at the submillisecond time scale. While previous work indicated that these cells receive no inhibitory inputs, the present study unambiguously demonstrates that these cells receive inhibitory glycinergic inputs. The physiologic impact of these inputs needs to be studied further. It remains **incomplete** at present but could be improved by addressing caveats related to similar sizes of excitatory postsynaptic potentials and spikes in the octopus neurons.

https://doi.org/10.7554/eLife.100492.1.sa2

Introduction

Perception depends on the ability of neurons to encode discrete features of complex external stimuli. These computations are determined by the type of information received from the periphery, the nature and position of the synapses, and the biophysical properties of the target neuron. For instance, in the auditory system, spiral ganglion neurons (SGNs) encode sound

information from hair cells in the cochlea and distribute it to specialized target neurons in the cochlear nucleus complex (CNC) that extract individual elements of the original sound, such as frequency, phase, intensity, and timing. The outcome of each dedicated computation continues to be processed through parallel ascending pathways and ultimately to the cortex, where the auditory features are reassembled to generate a percept. Thus, understanding how these first computations are made is a key step towards deciphering the basis of perception.

To generate accurate percepts of complex auditory stimuli, neurons must compute both what frequencies are present and when those frequencies occur across multiple time scales. For instance, overlapping sound stimuli, such as two competing speakers in a noisy room, are perceptually distinguished by correctly binding together frequencies with coherent onsets that then continue to change together over time[1,2]. Such computations require coincidence detection that can accurately encode co-occurring frequencies with submillisecond precision. Frequency information is communicated by SGNs, whose auditory nerve fibers (ANFs) project through the eighth nerve, bifurcate, and spread tonotopically to fill each division of the CNC (**Fig. 1A**). In addition, SGNs fall into physiologically distinct subtypes that are recruited at different intensities, thereby allowing sounds to be detected across a wide dynamic range and in the presence of background noise. Many target neurons receive SGN inputs from a limited range of frequencies and fire at the onset of the sound, effectively breaking it up into its frequency components. This presents a challenge for perception as auditory circuits must ultimately bind together co-occurring frequencies while also retaining information about their sequence to locate and recognize sounds.

In the mammalian auditory system, precise encoding of broadband timing information begins with the octopus cells of the CNC. Octopus cells are excitatory neurons that bind together co-occurring frequency information on a submillisecond timescale and send this information along one of the parallel ascending pathways in the auditory brainstem. Octopus cells are named for their large-diameter tentacle-like dendrites[3,4], which are oriented unidirectionally across a tonotopic array of SGNs such that each neuron integrates inputs from a wide range of frequencies[5–8]. SGNs provide the major excitatory inputs onto octopus cells. Biophysically, octopus cells have low input resistances near rest (~4MΩ), fast time constants (~200μs), and large low-voltage-activated potassium (~40nS at rest) and hyperpolarization activated (~62nS at rest) conductances. Together these properties give these cells impressively narrow windows of coincidence detection on the order of 1 millisecond[9–16]. This combination of receiving SGN innervation across broad frequencies and their biophysical specializations establish octopus cells as spectrotemporal coincidence detectors that can reliably encode the timing of complex stimuli, such as the broadband transients found in speech and other natural sounds[13,17,18]. Fittingly, *in vivo* recordings from octopus cells demonstrate their ability to phase lock to broadband transients at rates up to 1kHz[19–21]. Moreover, computational models of octopus cells demonstrate that onset responses are governed by the cell's biophysical specializations and are, in large part, the result of temporal summation of excitation[22–28]. The simplicity of its connectivity combined with the precision of its temporal computations makes the octopus cell an attractive model for understanding how specialized anatomical and electrophysiological properties contribute to neuronal computations.

Although the octopus cell's integration of SGN inputs within a very narrow time frame enables canonical coincidence detection, such a model does not explain how other temporal features of sound stimuli are encoded. Indeed, octopus cells encode spectrotemporal sequences within their broadly-tuned response areas, like frequency modulated sounds, that likely require further circuit specializations[29]. Although threshold somatic depolarization can be sufficient to activate an octopus cell[23], the vast majority of synapses are found on dendrites. Further, SGN inputs are organized tonotopically along octopus cell dendrites, with inputs from high frequency regions located more distal than those from low frequency regions. Dendritic morphology, passive cable properties, active resting membrane properties, and the spatial and temporal relationship

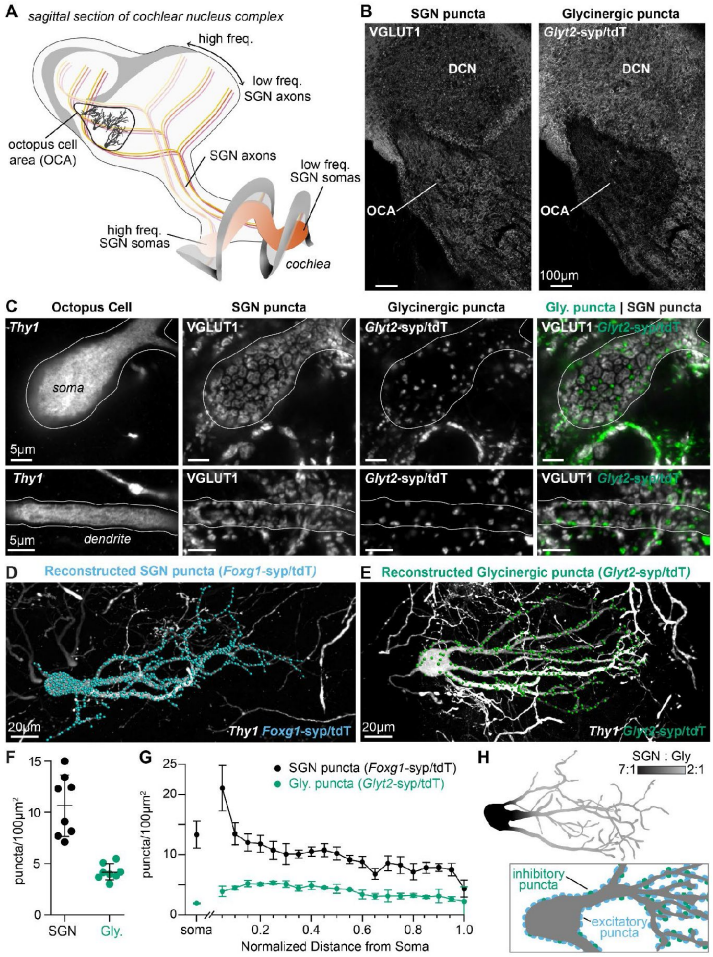

Figure 1.

Excitatory and inhibitory synapses to octopus cells form two domains.

(A) Illustration of spiral ganglion neuron (SGN) central axons branching within a parasagittal section of the mouse cochlear nucleus complex (CNC). SGN somas in the cochlea are tono-topically organized according to frequency. Axons remain organized throughout the ventral (VCN) and dorsal (DCN) divisions of the CNC. Octopus cells (inset) are found in the octopus cell area (OCA) of the VCN. **(B)** Excitatory SGN puncta labeled with a VGLUT1 antibody (left) and glycinergic puncta labeled with *Glyt2*^{Cre}-dependent syp/tdT (*Glyt2*-syp/tdT; right) in a par-asagittal section of the CNC. The teardrop-shaped OCA is not devoid of inhibitory inputs, although less prominent than in the surrounding CNC. **(C)** A *Thy1* sparsely labeled octopus cell with excitatory SGN (VGLUT1) and inhibitory (*Glyt2*-syp/tdT) puncta. Micrographs of 3µm confocal z-stacks show puncta on the medial surface of a soma (top) and a dendrite (bottom). **(D)** Representative reconstruction of excitatory SGN puncta labeled with *Foxg1*^{Cre}-dependent syp/tdT (*Foxg1*-syp/tdT; blue) onto a *Thy1*+ octopus cell. **(E)** Representative reconstruction of inhibitory puncta labeled with *Glyt2*-syp/tdT (green) onto a *Thy1* sparsely labeled octopus cell (white). **(F)** Puncta density for excitatory SGN (*Foxg1*-syp/tdT; black: 10.7 ± 3.0, *n* = 8 cells, 4 mice) and glycinergic puncta (*Glyt2*-syp/tdT; green: 4.2 ± 0.8, *n* = 8 cells, 3 mice) on octopus cell dendrites. Data are presented as mean ± SD. **(G)** Puncta density on somas for excitatory SGN (black: 13.3 ± 2.2, *n* = 8 cells, 4 mice) and glycinergic puncta (green: 1.8 ± 0.1, *n* = 8 cells, 3 mice) and the density along the length of dendrites. Data are presented as mean ± SEM. **(H)** *Top:* Illustration of an octopus cell and the ratio between excitatory SGN puncta and glycinergic puncta. *Inset:* Illustration of an octopus cell and the relative innervation densities of excitatory SGNs (blue) and inhibitory puncta (green).

between synaptic inputs can all impact excitatory post synaptic potential (EPSP) summation as excitation sweeps across the dendritic arbor and towards the soma. This raises the possibility that computations made in the dendrites influence the effective window of coincidence detection by the octopus cell. Such mechanisms could enable flexible processing that is adaptive to the dynamics of the environment without compromising the fidelity of high-fidelity coincidence computations.

Here, we sought to define the circuit mechanisms that allow octopus cells to act as coincidence detectors across time scales. We generated a comprehensive anatomical and physiological map of excitatory and synaptic inputs onto octopus cell somas and dendrites and examined how this circuit organization influences octopus cell activation. Through a combination of *in vitro* experiments and computational modeling, we show that the somatic summation of excitation is shaped by dendritic inhibition. Thus, octopus cells depend on compartmentalized computations that enable preservation of timing information both at the moment of stimulus onset and within an extended window for evidence accumulation, which is fundamental for the spectrotemporal integration of natural auditory stimuli.

Results

The balance of excitatory and inhibitory synapses is different in somatic and dendritic domains

To determine the wiring pattern that drives octopus cell computations, we generated a detailed map of excitatory and inhibitory synaptic inputs (**Fig. 1**). Overall, octopus cells receive abundant excitatory VGLUT1+ innervation from SGNs[30,31] and sparse inhibitory innervation from glycinergic neurons, as visualized using the glycinergic Cre driver *Glyt2*^{Cre} and the Ai34 synaptophysin-tdTomato (syp/tdT) fusion protein reporter (**Fig. 1B**). In addition, sparse inhibitory inputs nestle between SGN inputs, especially on octopus cell dendrites (**Fig. 1C**).

Quantification of the number and distribution of presynaptic puncta onto octopus cells revealed marked differences in the ratio of excitation and inhibition in the somatic and dendritic compartments. Since innervation patterns have never been systematically analyzed, we made three-dimensional reconstructions of 16 octopus cells and their excitatory SGN (n = 8 cells, 4 mice) and inhibitory (n = 8 cells, 3 mice) inputs. Octopus cells were visualized using a *Thy1* reporter and presynaptic puncta were labeled with the syp/tdT reporter driven either by *Foxg1*^{Cre} (**Fig. 1D**) or *Glyt2*^{Cre} (**Fig. 1E**). Consistent with qualitative assessment, the density of SGN inputs was higher (10.7 ± 3.0 SGN puncta/100µm^2) than that of inhibitory inputs (4.2 ± 0.8 puncta/100µm^2, **Fig. 1F**). Moreover, the relative proportions of excitatory and inhibitory inputs differed in the soma and dendrites (**Fig. 1G**). On somas, SGNs provided dense innervation that continued on the proximal dendrite, then gradually declined with distance from the soma. By contrast, somas received very few inhibitory inputs. On dendrites, inhibitory puncta were evenly distributed. As a result, octopus cells have a strikingly different average ratio of excitatory and inhibitory puncta on the soma (7:1) and on the dendrite (5:2), suggesting that each compartment contributes differentially to the final computation made by the octopus cell (**Fig. 1H**).

The majority of excitatory synapses on octopus cells are from type Ia SGNs

Although uniformly glutamatergic, SGNs exhibit stereotyped physiological differences in response thresholds that could affect the nature of their inputs onto octopus cells and influence octopus cell coincidence detection[32–35,35,36]. It was recently discovered that there are three molecularly distinct SGN subtypes, referred to as Ia, Ib, and Ic SGNs, which correlate with previously shown physiological groups[37–43] (**Fig. 2A**). Therefore, we further categorized

excitatory inputs based on SGN subtype identity. These can be identified with the presence of *Ntng1*-dependent reporter expression[44] in Ib and Ic SGNs (Ib/c) and its absence in Ia SGNs[40,41,43], coupled with very low to undetectable levels of calretinin (CR-) in Ic SGNs, and moderate to high levels of calretinin (CR+, CR++) in Ib and Ia SGNs (**Fig. 2B**). *Ntng1*^{Cre}-labeled Ib/c SGNs accounted for 60.1 ± 2.6% of the entire population, with 28.5 ± 12.2% Ib SGNs, 31.6% Ic SGNs, and 39.9 ± 2.6% Ia SGNs (**Fig. 2C**: n = 1599 neurons, 4 mice; mean ± SD). Further, proportions of SGN subtypes matched scRNA-seq estimates (**Fig. 2C**), indicating that this approach provides full coverage. SGN subtype identity was further confirmed by examining the spatial organization of SGN peripheral processes *en route* to the IHCs in the cochlea (**Fig 2A**, **Supp. Fig. 1A-C**).

Within the ventral cochlear nucleus (VCN), where octopus cells reside, *Ntng1*^{Cre} labeling was restricted to SGNs (**Supp. Fig. 1D**). In the VCN, expression of *Ntng1*-tdT and CR in SGN central axons was consistent with the moderate to undetectable levels of CR in *Ntng1*-tdT SGN somas in the periphery (**Supp. Fig. 2E**). Thus, *Ntng1*^{Cre}-driven expression of syp/tdT is an appropriate tool for mapping subtype-specific connectivity onto octopus cells.

Reconstruction of *Ntng1*^{Cre}-labeled Ib/c puncta (**Fig. 2D**) demonstrated that octopus cells are dominated by inputs from Ia SGN fibers, which are the fibers with the lowest response thresholds and highest rates of spontaneous activity. Octopus cell dendrites received 4.1 ± 1.0 puncta/100μm^2 from Ib/c SGNs (**Fig. 2E**, magenta: n = 9 cells, 5 mice; mean ± SD), accounting for 38% of the total SGN density. Given that *Ntng1*-tdT+ cells account for 60.1% of the SGN population (**Fig. 2C**, magenta), Ib/c inputs were underrepresented on octopus cells. Octopus cells receive similarly low innervation from Ic inputs (**Supp. Fig. 2G-I**: n = 6 cells, 2 mice), as estimated from the degree of sparse labeling of Ic axons achieved by *Myo15*^{iCre} reporter expression (**Supp. Fig. 2A-F**) and the expected proportion of Ic SGNs in the ganglion (**Supp. Fig. 2F**). By contrast, Ia SGNs, which comprise only ~40% of the total population (**Fig. 2C**, yellow), accounted for 62 ± 9.7% of SGN synapses on octopus cells (**Fig. 2E**, yellow: 6.6 ± 1.0 puncta/100μm^2). All three subtypes showed the same overall distribution from the soma to the distal dendrite (**Fig. 2F**). Together, excitatory and inhibitory puncta densities in the innervation maps indicate the average octopus cell receives ~1035 SGN synapses (642 Ia SGN, 393 Ib/c SGN) and ~354 inhibitory synapses. Additionally, the majority of synapses on the average octopus cell (83%) are found on dendrites, highlighting their critical role in the octopus cell computation.

Octopus cell reconstructions showed the same basic wiring patterns regardless of where each cell was positioned in the octopus cell area. The tonotopic position of all reconstructed octopus cell somas was estimated in 3D reconstructions aligned to a normalized CNC model of tonotopy[45]. Octopus cells had similar morphologies (**Supp. Fig. 3E-G**) and patterns of synaptic innervation (**Supp. Fig. 3H-M**) regardless of where they were positioned along the tonotopic axis. Thus, we have established a wiring diagram that finds low threshold, Ia SGN synapses to be the primary input to both the soma and dendrites of octopus cells. Additionally, the whole-neuron wiring diagram identifies a dendritic domain where inhibitory synapses are approximately equal in number to the Ib/c excitatory synapses from the periphery.

SGN inputs to octopus cells facilitate at high stimulation frequencies

Whether or not an octopus cell responds to its inputs depends on when and how EPSPs travel to and then summate in the soma. To determine if SGN subtypes transmit information differently to their central targets, we performed *in vitro* whole-cell current clamp recordings of octopus cells (**Fig. 3A**) while using Channelrhodopsin-2 (ChR2) to stimulate either all SGNs (*Foxg1*-ChR2) or only Ib/c SGNs (*Ntng1*-ChR2). Trains of ChR2-evoked SGN stimulation, ranging from 5 to 50Hz, in both the total SGN population (**Fig. 3B**, black: n = 8 cells, 5 mice) and the Ib/c SGN population

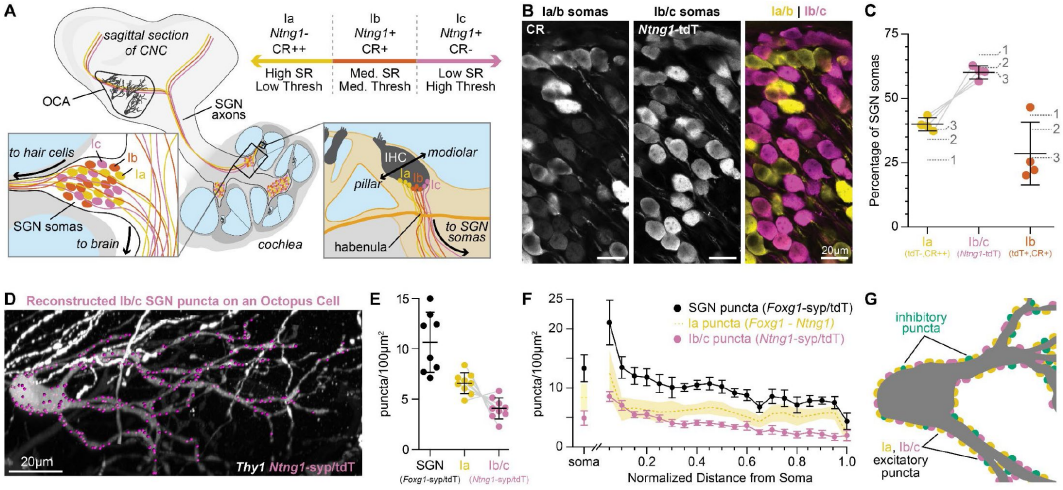

Figure 2.

Type Ia SGNs are the primary excitatory contributors to octopus cells.

(A) Ia (yellow), Ib (orange), and Ic (magenta) SGN axons innervate the CNC. SGNs have a continuum of properties organized along the pillar-modiolar axis of inner hair cells (IHCs) and the habenula. *Ntng1*-expressing Ib/c fibers are positioned on the modiolar side (closest to the ganglion). Strongly calretinin immunopositive Ia fibers are on the other side (closest to the pillar cells). This organization correlates with spontaneous rates (SR) and thresholds (thresh.) measured *in vivo*. Somas of all SGN subtypes are found at all tonotopic locations. **(B)** Calretinin (CR) immunolabeling distinguishes SGN subtypes. Ia/b somas label with high (CR++) and medium (CR+) levels of CR, respectively. Ic somas label with low to undetectable levels of CR (CR-). *Ntng1*^{Cre}-mediated expression of tdT (*Ntng1*-tdT) labels Ib/c SGNs. **(C)** Ias (tdT-, CR++) make up 39.9 ± 2.6% of the SGN population. Ib/cs (tdT+) make up 60.1 ± 2.6% of the SGN population. Ibs (tdT+CR+) make up 28.5 ± 12.2% of the SGN population (*n* = 1599 neurons, 4 mice). Data are mean ± SD; individual points represent percent coverage per animal, lines connect measurements from the same animal. Dotted lines indicate percentages from 1: Petitpré et al. 2018, 2: Shrestha et al. 2018, and 3: Sun et al. 2018. **(D)** Reconstructed Ib/c puncta labeled with *Ntng1*^{Cre}-dependent syp/tdT (*Ntng1*-syp/tdT; magenta) onto a *Thy1*+ octopus cell. **(E)** Puncta density for all SGNs (*Foxg1*-syp/tdT; black: data from **Fig. 1F**), Ias (*Foxg1* -*Ntng1*; yellow: 6.6 ± 1.0), and Ib/cs (*Ntng1*-syp/tdT; magenta: 4.1 ± 1.0, *n* = 9 cells, 5 mice) along the total dendritic length. Ia density was calculated by subtracting Ib/c density from total SGN density; lines connect measurements from the same reconstruction. Data are mean ± SD. **(F)** Puncta density on somas for all SGNs (*Foxg1*-syp/tdT; black: data from **Fig. 1E**), Ias (*Foxg1* -*Ntng1*; yellow: 8.4 ± 2.3), and Ib/cs (*Ntng1*-syp/tdT; magenta: 4.9 ± 1.2, *n* = 9 cells, 5 mice) and the density along the length of dendrites. Data are mean ± SEM. **(G)** Relative innervation densities of Ias (yellow), Ib/cs (magenta), and inhibitory puncta (green).

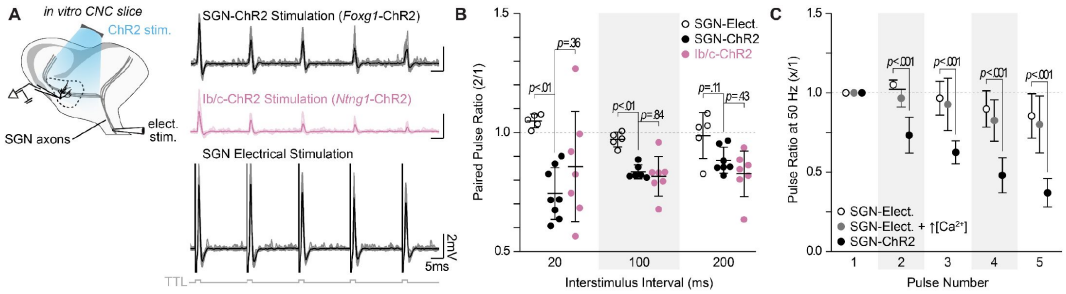

Figure 3.

SGN subtype inputs to octopus cells do not differ in short term plasticity.

(A) Illustration of the experimental paradigm and representative EPSPs recorded during *in vitro* whole-cell current clamp recordings of octopus cells. SGN stimulation method included electrical stimulation or full-field, light-evoked activation of *Foxg*-ChR2 or *Ntng1*-ChR2 SGNs. TTL trigger pulses are shown in gray. **(B)** Paired pulse ratios for electrically stimulated SGNs (open circles: n = 5 cells, 3 mice), ChR2 stimulated SGNs (*Foxg1*-ChR2; black: n = 8 cells, 5 mice), and ChR2 stimulated Ib/c SGNs (*Ntng1*-ChR2; magenta: n = 7 cells, 6 mice) at three interstimulus intervals. With electrical stimulation, SGN inputs to octopus cells were stable and exhibited slight facilitation at 50 Hz (20ms interstimulus interval). ChR2 stimulation caused paired pulse depression not seen with electrical stimulation. Data are presented as mean ± SD. Each data point represents the average paired pulse ratio for a cell. p values from ANOVA and subsequent Tukey HSD test are reported for comparisons between methods of SGN activation (electrical and ChR2) and SGN subpopulation composition within method of activation (SGN-ChR2 and Ib/c-ChR2). Welch's ANOVA was used for comparisons at 20ms interstimulus interval (50Hz) as data in this condition did not meet the homogeneity of variance assumption. **(C)** Pulse ratios at 50Hz for electrically stimulated SGNs with physiological 1.4mM Ca^{2+} ACSF (open circles: n = 5 cells, 3 mice), electrically stimulated SGNs with 2.4mM Ca^{2+} ACSF (grey: n = 3 cells, 2 mice) and ChR2 stimulated SGNs with physiological ACSF (*Foxg1*-ChR2; black: n = 8 cells, 5 mice). Data are presented as mean ± SD. $p < 0.001$ from ANOVA and subsequent Tukey HSD test for all comparisons between methods of SGN activation (electrical and ChR2). There were no statistically significant differences for all comparisons under 1.4mM and 2.4mM Ca^{2+} ($p > 0.100$, ANOVA).

(**Fig. 3B**, magenta: *n* = 7 cells, 6 mice) exhibited no differences in paired-pulse plasticity at any frequency of stimulation (p > 0.35 at all interstimulus intervals, Tukey's HSD), although the Ib/c population exhibited higher variability than the total SGN population (at 20ms: SD = 0.11, SD = 0.24, respectively).

ChR2-evoked synaptic responses are known to artificially undergo synaptic depression[46,47]. To determine if the paired pulse depression measured in ChR2-stimulated experiments was physiological (**Fig. 3B**), we used electrical stimulation to evoke EPSPs from SGNs. Electrically-evoked SGN EPSPs had higher paired-pulse ratios than ChR2-evoked EPSPs and were mildly facilitating at short (20ms) intervals (**Fig. 3B-C**, open circles: *n* = 5 cells, 3 mice), consistent with an octopus cell's ability to respond reliably to click trains *in vivo*[5,7,20,48]. In contrast, previous results using electrical stimulation demonstrated short-term depression of SGN inputs to octopus cells[49,50]. However, these experiments were carried out in the presence of higher, non-physiological levels of extracellular calcium. We repeated paired pulse plasticity experiments with non-physiological calcium concentrations (2.4mM) and similarly found that electrically-evoked EP-SPs from SGNs resulted in short-term depression at 50Hz of electrical stimulation (**Fig. 3C**, grey: *n* = 3 cells, 2 mice), though not to the degree observed when using full-field, ChR2-evoked inputs.

Glycine evokes inhibitory post synaptic potentials that are occluded by a low input resistance

Given the increased density of inhibitory synapses on octopus cell dendrites, we considered the possibility that somatic and dendritic compartments contribute differently to the temporal computation made by octopus cells. A role for inhibition has never been incorporated into octopus cell models as previous efforts failed to reveal physiological evidence of functional inhibitory synapses onto octopus cells either *in vitro*[12,51,52] or *in vivo*[29]. Similarly, we did not observe light-evoked (*Glyt2*-ChR2*)* inhibitory post synaptic potentials (IPSPs) in octopus cell somas during whole-cell current clamp recordings from P30-45 mice. Since inhibitory synapses are located primarily on octopus cell dendrites, we posited that their voltage spread to the soma is limited given the extremely low input resistance of octopus cell somas.

To decrease electrotonic isolation of the dendrites and increase input resistance, we pharmacologically blocked voltagegated potassium (K_v) and hyperpolarization-activated cyclic nucleotide-gated (HCN) channels using 100µM 4-Aminopyridine (4-AP) and 50µM ZD 7288 (ZD). This cocktail increased octopus cell membrane resistance (**Fig. 4A**). To isolate inhibition, 15µM 2,3-dioxo-6-nitro-7-sulfamoyl-benzo[f]quinoxaline (NBQX) was added to block AMPA receptor activation. Consistent with our hypothesis, the increase in input resistance unveiled light-evoked IPSPs in recordings from octopus cell somas (**Fig. 4B**). Bath application of 500nM strychnine (STN) fully abolished IPSPs (**Fig. 4C**), confirming functional glycinergic inhibitory synaptic transmission onto octopus cells.

To determine the types of glycinergic receptors contributing to IPSPs, we pharmacologically blocked subsets of glycine receptors (**Fig. 4C**). IPSPs were reduced upon addition of 20µM picrotoxin (PTX), which blocks homomeric glycine receptors[53–55]. Sequential addition of 100µM cyclothiazide (CTZ), which blocks α2-containing homomeric and heteromeric glycine receptors[56,57], nearly abolished the remaining IPSPs, and responses were fully abolished with further application of 500nM STN. Collectively, these data demonstrate that glycinergic synaptic contacts onto octopus cell dendrites are functional. Additionally, glycine receptor subunit composition (**Fig. 4C**) implicates a role for both large conductance extrasynaptic β-subunit lacking homomeric receptors and synaptically localized α2β receptors with slower kinetics[58–60].

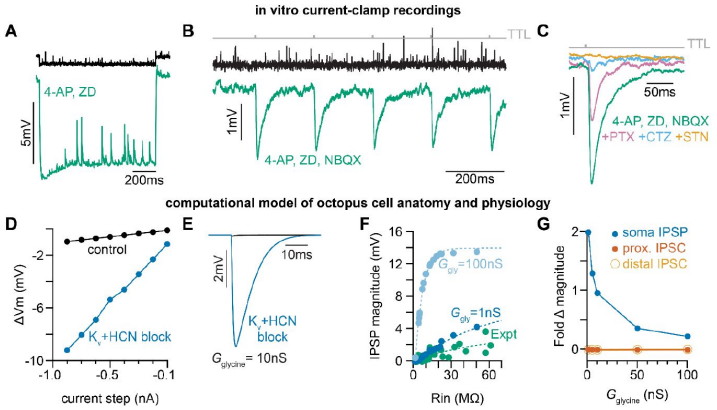

Figure 4.

Octopus cells receive glycinergic inhibitory post synaptic potentials.

(A) Voltage responses to a -200pA current injection. This representative neuron hyperpolarized 0.7mV (black) in control conditions. After bath application of 100μM 4-Aminopyridine (4-AP) and 50μM ZD 7288 (ZD), hyperpolarizing responses to the same -200pA current injection increased to 8.8mV at steady state (green). **(B)** Postsynaptic responses to ChR2 stimulation of glycinergic terminals (*Glyt2*-ChR2*)* with a 5Hz train (gray) of 1ms full-field blue light pulses before (black) and after bath application of 100μM 4-AP, 50μM ZD, and 15μM NBQX (green: *n* = 9 cells, 8 mice). Increased input resistance reveals inhibitory potentials that are difficult to detect. **(C)** Postsynaptic responses to *Glyt2*-ChR2 stimulation after bath application of 100μM 4-AP, 50μM ZD, and 15μM NBQX (green), with further sequential addition of 20μM picrotoxin (PTX, pink), 100μM cyclothiazide (CTZ, blue), and 500nM strychnine (STN, orange; *n* = 6 cells, 5 mice). **(D)** Change in membrane voltage in response to hyperpolarizing somatic current steps in a morphologically and biophysically realistic model of octopus cells before (black) and after removal of voltage-gated potassium (K_V) and hyperpolarization-activated cyclic nucleotide-gated (HCN) channels (blue). As in *in vitro* current-clamp recordings, removing K_V and HCN channels increased the magnitude of voltage responses (ΔVm) to hyperpolarizing current. **(E)** IPSPs measured at the soma of a modeled octopus cell before (black) and after removal of K_V and HCN channels (blue). As in *in vitro* current-clamp recordings, this allows for somatic IPSP detection. **(F)** IPSP magnitude in experimental data (green) and the model (blues) as a function of input resistance. In somatic measurements, IPSP size increases with input resistance. Modeled IPSPs are shown for two conductance levels (1nS, dark blue; 100nS light blue). **(G)** Fold change in magnitude of soma-measured IPSPs (blue) or dendrite-measured IPSCs at proximal (dark orange) and distal (light orange) dendritic locations after removal of K_V and HCN channels. K_V and HCN block increases the magnitude of soma-measured IPSPs. The size of dendritic IPSCs are not changed with K_V and HCN or synapse location.

To confirm whether the confinement of IPSPs to the dendrites is consistent with our understanding of octopus cell biophysics, we developed an improved biophysically and anatomically accurate model of octopus cells based on our findings (**Supp. Fig. 4**)[18,61]. This model performed as predicted based on our experimental results. As in our current-clamp recordings (**Fig. 4A**), removal of K^V and HCN conductances in the model changed the input resistance and current-voltage relationship of the neuron, resulting in reduced electronic isolation (**Fig. 4D**, blue). In control conditions, stimulation of dendritic glycinergic conductances induced negligible hyperpolarizing voltage changes (**Fig. 4E**, black). With increased input resistance, dendritic IPSPs measured at the soma were similar to *in vitro* recordings (**Fig. 4E-F**). Thus, this model confirms that dendritic IPSPs can elicit somatic hyperpolarization in octopus cells when electrotonic dendritic isolation is reduced.

While blocking K_v and HCN allowed us to reveal IPSPs at the soma, 4-AP increases the duration of the already unphysiological ChR2-evoked presynaptic action potential[47], resulting in altered release probabilities and synaptic properties, amongst other caveats[62]. To directly confirm that the increase in somatically-measured IPSP amplitude can be explained by changes in input resistance alone, we used the octopus cell model to simulate dendritic glycinergic conductances and measure changes in dendritic current and somatic potential amplitude in the presence of blocked K_v and HCN channels. K_v and HCN block and the resulting change in input resistance increased the magnitude of soma-measured IPSPs for all glycine conductances (**Fig. 4G**, blue). Dendrite-measured currents did not change as a result of the hyperpolarization induced by K_v and HCN block regardless of synaptic location on the dendrites or the magnitude of the glycine conductance (**Fig 4G**, dark orange, light orange). Together, results from the model replicate those collected *in vitro* and provide evidence of functional glycinergic synaptic transmission that is difficult to detect with *in vitro* somatic recordings.

Inhibition decreases the magnitude and advances the timing of dendritic SGN inputs

SGN synapses onto octopus cell dendrites are arranged tonotopically, with higher frequency SGNs from the base of the cochlea terminating on the distal dendrites and lower frequency SGNs from more apical positions terminating more proximally (**Fig. 1A**). This organization has been proposed to re-synchronize coincidentally firing SGNs that are activated at slightly different times due to the time it takes for the sound stimulus to travel from the base to the apex of the cochlea[18]. To test how inhibition in the dendrites shapes coincidence detection, we first used our model to explore the influence of simultaneous activation of inhibitory and excitatory synapses at varying locations along the dendritic tree. By placing inhibitory synapses on proximal or distal dendrites and moving the relative location of excitation, we modelled the effect of on-path and off-path inhibition[63] on somatically recorded EPSPs (**Fig. 5A**, **Supp. Fig. 5**). For both inhibition proximal to excitation (**Fig. 5B-C**: on-path) and inhibition distal to excitation (**Fig. 5D-E**: off-path), the model predicted that inhibition reduces EPSP amplitude and accelerates EPSP peak timing at the soma. Thus, the presence of inhibition appears to enable modulation of EPSP timing in dendritic compartments during continuous auditory stimuli when inhibition can be recruited beyond the onset of a sound and thus allow for adaptable temporal processing during the duration of a stimulus.

To directly test if the model's prediction that temporally coincident excitation and inhibition affects the timing and amplitude of excitatory SGN inputs as they travel towards the octopus cell soma, we coincidently activated SGNs and glycinergic inputs *in vitro*. In these experiments, the octopus cell properties were not altered pharmacologically and inhibition was undetectable or only visible with averaging over many sweeps (**Fig. 5F**, blue). When synaptic inhibition was evoked together with excitation (**Fig. 5F**, green), the soma-recorded EPSPs were smaller than when excitation was evoked alone (**Fig. 5F**, black: n = 8 cells, 6 mice). ChR2-evoked inhibition decreased EPSP heights by 25.2 ± 9.0% (**Fig. 5G**, green) and shifted the peak of EPSPs forward

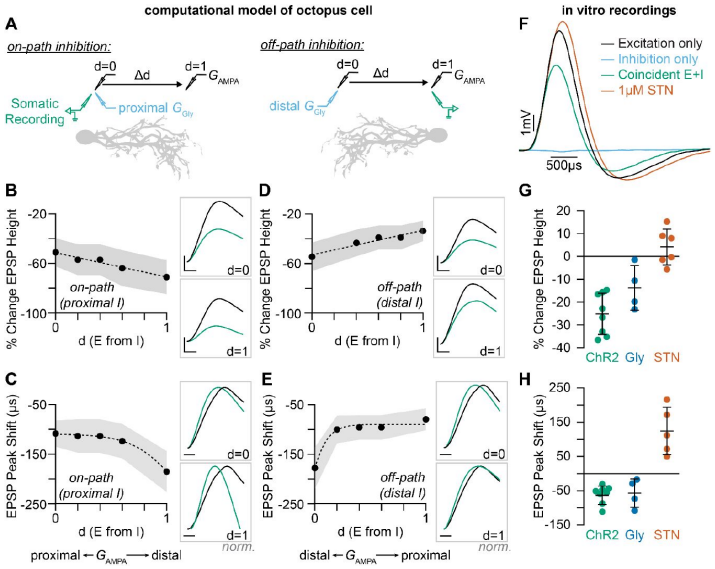

Figure 5.

Coincident excitation and inhibition on octopus cell dendrites advances EPSP peak times.

(A) The impact of distance between excitatory and inhibitory synapses was measured in a computational model of octopus cells. Inhibitory synapses were placed either proximally (on-path) or distally (off-path) to excitation. Excitatory synapses were placed at varying locations along the dendritic arbor to change the anatomical distance (Δd) where d=0 is the location of inhibition (G_{Gly}) and d=1 is the condition where excitation (G_{AMPA}) and inhibition are maximally separated. EPSPs were measured at the soma in all conditions (green). **(B-E)** Quantification of the percent change in soma-measured EPSP magnitude and the shift in EPSP peak timing in models of *(B-C)* on-path and *(D-E)* off-path inhibition. Example traces show EPSPs with (green) and without (black) inhibition at d=0 and d=1. Distal dendrites (d=1) have higher local input resistance and lower IPSP attenuation due to the sealed end. Inset scale bars are 1mV, 200ms. **(F-H)** Coincident stimulation of excitation and inhibition changes EPSP shape. (*F)* Representative responses to independent stimulation of excitatory SGNs (black), independent stimulation of inhibitory inputs (light blue), coincident stimulation of both excitation and inhibition (green), and independent stimulation of excitatory SGNs with the addition of 1μM strychnine (STN). Quantification of *(G)* the percent change in EPSP height and *(H)* the shift in EPSP peak timing during coincident *Glyt2*-ChR2 activation of inhibitory inputs (green: *n* = 8 cells, 6 mice), bath application of 25μM glycine (dark blue: *n* = 4 cells, 3 mice), and bath application of 1μM STN (orange: *n* = 5 cells, 4 mice). Activation of glycinergic receptors during excitation decreases EPSP heights and advances EPSP peaks. Blocking of tonically active glycine receptors slows and delays EPSPs. Data are presented as mean ± SD. Markers represent the average quantification for a cell.

57.5 ± 26μs (**Fig. 5H**, green). This effect was mimicked by bath application of 25μM glycine (**Fig. 5G-H**, blue: n = 4 cells, 3 mice). Further, bath application of 1μM STN had the opposite effect, resulting in larger EPSPs, delayed peak times, and increased half-widths (**Fig. 5F-H**, orange: n = 5 cells, 4 mice). Thus, the timing of EPSP arrival may be shaped both by the release of synaptic glycine and by tonically active glycine channels. Of note, many SGNs also terminate on the octopus cell soma, where inhibition is minimal. This suggests that the octopus cell's ability to act as a coincidence detector depends on two stages of compartmentalized computations, one in the dendrite that combines excitation and inhibition to provide important information about which frequencies co-occur in a complex sound stimulus and one in the soma that is restricted by the rigid temporal summation window for coincidence detection. Together with the electrotonic properties of the octopus cell and the dominance of low threshold, low jitter Ia SGN inputs, these combined computations can enable reliable coincidence detection and proper cross-frequency binding needed for perception of sound.

Discussion

Coincidence detection plays a critical role in many cognitive and perceptual processes, from the ability to localize sound, to the binding of auditory and visual features of a common stimulus. Depending on the computation, the temporal window for integration can range widely, thereby requiring circuitry with distinct anatomical and physiological properties. Here, we describe a two-domain mechanism for coincidence detection that can detect co-occurring frequencies with different degrees of precision. By mapping and selectively activating synaptic inputs onto octopus cells both *in vitro* and in a computational model, we revealed that compartmentalized dendritic nonlinearities impact the temporal integration window under which somatic coincidence detection computations are made. The arrival of many small, reliable excitatory inputs (**Fig. 3**) from low-threshold SGNs (**Fig. 2**) is continuous throughout an ongoing stimulus. We demonstrate that glycinergic inhibition to octopus cell dendrites (**Fig. 1**) can shift the magnitude and timing of SGN EPSPs as they summate in the soma (**Fig. 4**,**5**). The narrow window for coincidence detection computations allows the octopus cell to respond with temporal precision using momentary evidence provided by SGNs at the onset of the stimulus. We propose that, as a stimulus persists, inhibition onto octopus cell dendrites can adjust the timing of excitation before arriving at the soma for the final input-output computation. This allows the cell to make an additional computation with a slightly longer window for evidence accumulation without compromising the accuracy of the somatic onset computation (**Fig. 6**).

As coincidence detectors in the auditory system, octopus cells are faced with the challenge of recognizing complex sounds that include many frequencies that co-occur from the beginning to the end of the stimulus. As shown by *in vivo* recordings[6,29], octopus cells respond well to cues that include complex spectrotemporal patterns, including frequency modulations beyond the onset of the stimulus[29]. Given that the auditory environment is filled with overlapping sound stimuli, such responses presumably allow the octopus cell to encode which frequencies belong to which sound. Our data thus support the role of octopus cells beyond simple onset coincidence detectors that rely solely on the temporal summation of excitation. The results suggest that, despite high K_v and HCN conductances at rest, the addition of dendritic inhibition transforms the magnitude and timing of SGN signals as they arrive in the cell body, which may expand their response selectivity and allow them to become a slightly leakier integrator and thus accumulate evidence beyond onsets. Although, this inhibition is difficult to detect because of shunting, our data demonstrate that it is both present and impactful.

As well as needing to work beyond onsets, an effective coincidence detector in the auditory system must also function reliably across a range of sound intensities. Intensity information is encoded by the number and types of SGNs that are activated in the cochlea. The Ia, Ib, and Ic molecular subtypes defined in mouse[40,41,43] broadly correspond to the anatomically and

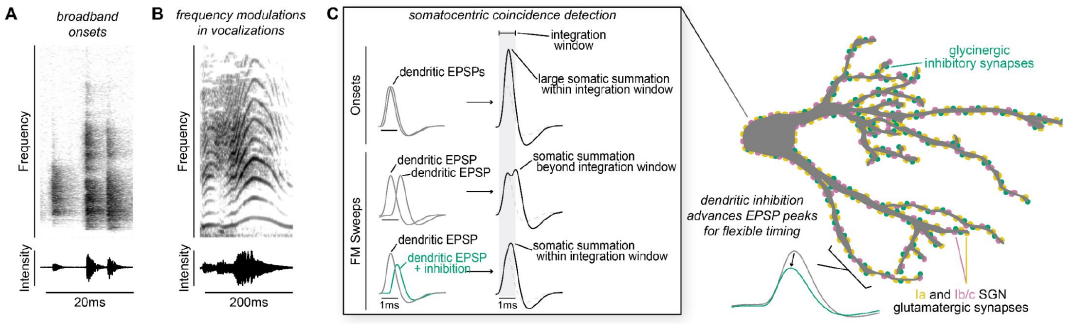

Figure 6.

Proposed model of flexible dendritic timing for precise somatic coincidence detection.

(A-B) Co-occurring frequencies in broadband onsets and frequency modulations occur on different time scales. *(Top)* Spectrograms illustrate frequency strength over time. *(Bottom)* Waveform illustrate total intensity over time. Both of these stimuli drive firing in octopus cells despite the limitations imposed by a ~1ms window for temporal integration. **(C)** Excitation must summate at the soma of octopus cells within a narrow time window (~1ms) to achieve a depolarization rate rapid enough to trigger action potentials. Summation of excitation alone accounts for responses to sound onsets (inset, top). Stimuli that require summation over a longer time period, such as frequency modulated sweeps, require synaptic inhibition to modulate the timing of excitation on octopus cell dendrites before they reach the soma for coincidence detection computations (inset, bottom). We propose a mechanism for preferential processing of a subset of excitatory inputs where selective temporal advancement of a subset of EPSPs could expand the effective window for coincidence detection at the soma.

physiologically defined subtypes described across species[42,64]. We find that the majority of inputs onto octopus cells come from Ia SGNs, which most closely correspond to the low-threshold, high-spontaneous rate population. Consistent with this result, single-unit SGN recordings in cats demonstrated a bias towards low-threshold, high-spontaneous rate axon collaterals in the octopus cell area[33]. Low-threshold SGNs are also characterized by short first spike latencies and low temporal jitter[65–68]. A hallmark of the octopus cell is the fact that it only fires action potentials when many SGN inputs are activated within a narrow period of time[69]. The presence of many low-threshold and temporally precise inputs on the octopus cell may help ensure that coincidence detection still works reliably for quiet sounds. Further, Ia inputs onto octopus cells do not exhibit paired-pulse depression, not unlike low levels of depression seen in Ia inputs to bushy cells[70]. The presence of SGN inputs without paired-pulse depression could be beneficial for encoding sustained auditory signals. Finally, although Ia SGNs are over-represented, Ib and Ic inputs are also present. Since precise, low-threshold SGN responses can be saturated by background noise such that responses to relevant stimuli are masked[38,65,68,71], recruitment of higher threshold SGNs at higher sound intensities may compensate for this tradeoff.

The presence of inhibitory inputs onto dendrites is a fundamental feature of the nervous system and, in other systems, contributes to a neuron's final computation. For example, direction selectivity computations in dendrites of retinal cells require excitation-inhibition interactions in dendritic compartments[72,73]. In pyramidal cells of the cortex and hippocampus, the spatial distribution of inhibition impacts dendritic non-linearities in a branch selective manner[74–79]. However, octopus cells do not share all mechanisms for dendritic computation as neurons in the cortex and hippocampus. The lack of backpropagating action potentials and dendritic calcium spikes in octopus cells causes submillisecond timing differences in dendritic summation of coincident excitation and local inhibition to be consequential in subthreshold computation before somatic action potential generation.

Although this work uncovers a role for inhibition, understanding of octopus cell computations is limited by the fact that it remains unclear what kind of information is carried by inhibitory inputs. Although the presence of presynaptic glycinergic puncta in the octopus cell area[80–83] and glycinergic receptor expression in octopus cells[84–88] is well established, it is unknown where this glycinergic innervation originates. Of the local neurons within the CNC that provide inhibition to the VCN, there is no evidence of connections to octopus cells from D-Stellate[52], L-Stellate[89], or tuberculoventral cells[90]. Outside of the CNC, terminal degeneration experiments in cats suggested the superior periolivary nucleus (SPON) and the ventral division of the lateral lemniscus (VNLL) as potential sources of descending inhibition to the octopus cell area[91]. Octopus cells provide excitatory input to both the SPON[92–96] and the VNLL[20,97–101], raising the possibility of feedback inhibition from the auditory brainstem as a circuit mechanism for elongated temporal summation windows during ongoing stimuli. Although feedback inhibition is not rapid enough to prevent or alter the onset response that octopus cells are well-known for, it could limit the duration of a response or change the effective coincidence detection window as the stimulus continues. Future studies will be required to identify the source of inhibition and its organization along the dendrites. If inhibitory inputs tonotopically match the local, narrowly-tuned dendritic SGN inputs, it is possible that frequency matched inhibition could influence spectral selectivity or feature extraction. On the other hand, broadly tuned inhibition could reduce depolarization block or serve as a temporal milestone that signals gaps or offsets. Further characterization of *in vivo* octopus cell responses in complex sound environments may clarify the effect of noise on signal detection and could reveal additional features of this cell's contributions to perception of the auditory world.

Acknowledgements

We thank Dr. Nace Golding (University of Texas at Austin), Dr. Matthew McGinley (Baylor College of Medicine), Dr. Phillip Joris (KU Leuven), and Dr. Bernardo Sabatini for helpful discussions and feedback. Sadie Quinn, Lucy Lee, and Ryan Merrow provided valuable technical assistance. Dr. Bruce Bean (Harvard Medical School) generously provided access to electrophysiological equipment. *Slc6a5*$^{tm1.1(Cre)Ksak}$ mice were kindly provided by Dr. Wade Regehr (Harvard Medical School). *Ntng1*$^{em1(Cre)Kfra}$ mice were made and kindly provided by Dr. Fan Wang (Massachusetts Institute of Technology). *Myo15a*$^{tm1.1(Cre)Ugds}$ mice were kindly provided by Dr. Stefan Heller (Stanford). We thank Rigoberto Ramirez, Tenzin Paljorwa, and Edgar Ramirez for animal care support. We are grateful to the Neurobiology Imaging Facility (NIF) for software availability and to the HMS Research Instrumentation Core for the design and fabrication of temperature regulation equipment. This work was supported by grants from the BRAIN Initiative 1R01NS118402 to L.V.G., the National Institute on Deafness and Other Communication Disorders 5R01DC009223 to L.V.G. and 1F32DC020070 to L.J.K, the William Randolph Hearst Fund to L.J.K, and the Broad Institute's Stanley Center for Psychiatric Research to S.H. and G.F.

Author Contributions

Conceptualization, L.J.K. and L.V.G.; Methodology, S.H.; Formal Analysis, L.J.K and S.H.; Investigation, L.J.K, S.M., and S.S.; Resources, G.F.; Writing, L.J.K. and L.V.G.; Visualization, L.J.K. and S.H.; Supervision, G.F. and L.V.G.; Funding Acquisition, L.J.K, G.F., and L.V.G. Declaration of Interests

Declaration of Interests

The authors declare no competing interests.

Materials and Methods

Animal Use and Transgenic Mouse Lines

All procedures were approved by and conducted in accordance with Harvard Medical School Institutional Animal Care and Use Committee. Male and female mice (*Mus musculus*) were bred on a C57BL/6 background at the Harvard Center for Comparative Medicine or obtained from Jackson Laboratories (Bar Harbor, ME). Mice were housed in groups of up to five animals and maintained on a 12hr light/dark cycle. Transgenic alleles were heterozygous for each transgene for all experimental animals. Descriptions of allele combinations for all experiments can be found in **Supplemental Table 1**.

Spiral ganglion neurons (SGNs) and their central auditory nerve fibers (ANFs) were targeted using either *Foxg1*$^{tm1.1(Cre)Ddmo}$ (*Foxg1*^{Cre})[102] or *Foxg1*^{Flp}, both of which drive robust reporter expression neurons in the auditory and vestibular ganglion[103,104] and the neocortex[105,106], but not in brainstem or midbrain neurons. *Foxg1*^{Flp} mice were generated by crossing the *Foxg1*$^{tm1.1Fsh}$ mouse line[107] with the Tg(EIIa-Cre)C5379Lmgd mouse line[108], then backcrossing to isolate the flp transgene and remove the Cre transgene.

Inhibitory inputs to octopus cells were targeted with *Slc6a5*$^{tm1.1(Cre)Ksak}$ mice (*Glyt2*^{Cre})[109].

Octopus cells were sparsely labeled with the Tg(Thy1-YFP)HJrs (*Thy1*) mouse line[110]. This line labels ~0-15 octopus cells amongst other neurons throughout the brain.

Ib/c SGNs were targeted using the *Ntng1*$^{em1(Cre)Kfra}$ (*Ntng1*^{Cre}) mouse line, which drives expression in neurons throughout the nervous system (**Supp. Fig. 1F**) and disrupts expression of the endogenous allele[44]. Auditory brainstem responses in adult *Ntng1*$^{Cre/+}$ mice are normal. Ic SGNs were sparsely targeted with the *Myo15a*$^{tm1.1(Cre)Ugds}$ (*Myo15*^{iCre}) mouse line[111].

Fluorescent reporters included *Gt(ROSA)26Sor*$^{tm14(CAG-tdTomato)}$ (Ai14, tdT)[112], *Gt(Rosa)26Sor*$^{tm34.1(CAG-Syp/tdTomato)}$ (Ai34, syp/tdT), and *Gt(Rosa)26Sor*$^{tm1.2(CAG-EGFP)Fsh}$ (RCE:FRT, EYFP)[113]. We also used *Gt(Rosa)26Sor*$^{tm32(CAG-COP4*H134R.EYFP)}$ (Ai32, ChR2)[114] to drive synaptic activity in *in vitro* slice experiments.

Histology and Reconstructions

For immunohistochemical labeling, mice were deeply anesthetized with isoflurane and transcardially perfused with 15mL of 4% paraformaldehyde (PFA) in 0.1M phosphate-buffered saline (PBS) using a peristaltic pump (Gilson). Whole skulls containing brain and cochlea were immediately transferred to 20mL of 4% PFA and post-fixed overnight at 4°C. Fixed brains and cochlea were removed from the skulls and washed with 0.1M PBS.

Brains were collected from mice of both sexes, aged 28-38 days, and embedded in gelatin-albumin hardened with 5% glutaraldehyde and 37% PFA[115]. Sections were cut at 35, 65, or 100µm with a vibrating microtome (Leica VT1000S) and free-floating tissue was collected in 0.1M PBS. For sections less than 65µm, tissue was permeabilized and nonspecific staining was blocked in a solution of 0.2% Triton X-100 and 5% normal donkey serum (NDS, RRID: AB_2337258) in 0.1M PBS for 1 hour. After blocking, tissue was treated with primary antibody in a solution containing 0.2% Triton X-100 and 5% NDS in PBS for 1-2 nights at room temperature. Primary antibodies used were: chicken anti-GFP (1:1000, RRID:AB_10000240), rabbit anti-RFP (1:1000, RRID:AB_2209751), goat anti-calretinin (1:1000, RRID:AB_1000034), and guinea pig anti-VGLUT1 (1:500, RRID:AB_887878). Sections were washed in 0.1M PBS then incubated in a secondary antibody solution (1:1000) containing 0.2% Triton X-100 and 5% NDS for 2-3hrs at room temperature. Tissue sections were mounted on charged slides and coverslipped (Vectashield Hardset Antifade Mounting Medium with DAPI), and imaged using a Zeiss Observer.Z1 confocal microscope.

For 100µm sections, tissue was washed in CUBIC-1A solution for 1hr for strong permeabilization and delipidization[116,117]. Tissue was then further permeabilized and nonspecific staining was blocked in a solution of 0.2% Triton X-100 and 5% NDS in 0.1M PBS for 1hr. After blocking, tissue was treated with primary antibody in a solution containing 0.2% Triton X-100 and 5% NDS in PBS for 4 nights at 37°C. Primary antibodies used were: chicken anti-GFP (1:1000, RRID:AB_10000240), and rabbit anti-RFP (1:1000, RRID:AB_2209751). Sections were then incubated in a secondary antibody solution (1:400) containing 0.2% Triton X-100 and 5% NDS for 4 nights at 37°C. Tissue sections were pre-incubated in CUBIC2 solution, then temporarily mounted on uncharged slides with CUBIC2 solution for immediate imaging using a Zeiss Observer.Z1 confocal microscope.

Octopus cells and synaptic puncta were reconstructed in Imaris (Oxford Instruments). YFP signal from the target octopus cell was used to generate a surface reconstruction and mask syp/tdT signal. Dendrites were reconstructed using the masked YFP signal and separated into 10µm increments. Masked syp/tdT puncta were marked and localized to a 10µm increment of the dendritic tree. Synapse counts, dendrite metrics, and masked channels were exported to Excel (Microsoft) for further analysis.

Cochlea were collected from mice of both sexes, aged 28-42 days. The bony labyrinth of the inner ear was decalcified in 0.5M ethylenediamine tetraacetic acid (EDTA) for 3 nights at 4°C and embedded in gelatin-albumin hardened with 5% glutaraldehyde and 37% PFA. Sections were cut at 65µm with a vibrating microtome (Leica VT1000S) and free-floating tissue was collected in 0.1M PBS. Sections were washed in CUBIC-1A solution for 1hr for strong permeabilization and delipidization. Tissue was further permeabilized and nonspecific staining was blocked in a solution of 0.2% Triton X-100 and 5% NDS in 0.1M PBS for 1hr. After blocking, tissue was treated with primary antibody in a solution containing 0.2% Triton X-100 and 5% NDS in PBS for 2 nights at room temperature. Primary antibodies used were: chicken anti-GFP (1:1000, RRID:AB_10000240), rabbit anti-RFP (1:1000, RRID:AB_2209751), goat anti-calretinin (1:1000, RRID:AB_1000034).

Sections were then incubated in a secondary antibody solution (1:500) containing 0.2% Triton X-100 and 5% normal goat serum for 2-3hrs at room temperature. Tissue sections were mounted on charged slides, coverslipped (Vectashield Hardset Antifade Mounting Medium with DAPI), and imaged using a Zeiss Observer.Z1 confocal microscope.

Acute Slice Electrophysiology

Data were obtained from mice of both sexes, aged 24-47 days. Mice were deeply anesthetized with isoflurane and perfused transcardially with 3mL of 35°C artificial cerebral spinal fluid (ACSF; 125mM NaCl, 25mM glucose, 25mM $NaHCO_3$, 2.5mM KCl, 1.25mM NaH_2PO_4, 1.4mM $CaCl_2$, and 1.6mM $MgSO_4$, pH adjusted to 7.45 with NaOH). For high calcium concentration experiments presented in **Fig. 3C**, ACSF contained 125mM NaCl, 25mM glucose, 25mM $NaHCO_3$, 2.5mM KCl, 1.25mM NaH_2PO_4, 2.4mM $CaCl_2$, and 1.3mM $MgSO_4$. Mice were rapidly decapitated and the brain was removed and immediately submerged in ACSF. Brains were bisected and 250µm slices were prepared in the sagittal plane with a vibrating microtome (Leica VT1200S; Leica Systems). Prepared slices were incubated for 30min at 35°C, then allowed to recover at room temperature for at least 30min. ACSF was continuously bubbled with 95% O_2/5% CO_2.

Whole-cell recordings were conducted at 35°C using a Multiclamp 700B (Molecular Devices) in current-clamp mode with experimenter adjusted and maintained bridge balance and capacitance compensation. Data were filtered at 12kHz, digitized at 83–100kHz, and acquired using pClamp9 (Molecular Devices). Neurons were visualized using infrared Dodt gradient contrast (Zeiss Examiner.D1; Zeiss Axiocam 305 mono). Glass recording electrodes (3–7MΩ) were wrapped in parafilm to reduce capacitance and filled with an intracellular solution containing 115mM K-gluconate, 4.42mM KCl, 0.5mM EGTA, 10mM HEPES, 10mM Na_2Phosphocreatine, 4mM MgATP, 0.3mM NaGTP, and 0.1% biocytin, osmolality adjusted to 300mmol/kg with sucrose, pH adjusted to 7.30 with KOH. All membrane potentials are corrected for a 11mV junction potential.

For optogenetic activation, full-field 470nm blue light was presented through a 20x immersion objective (Zeiss Examiner.D1). Onset, duration, and intensity of light was controlled by a Colibri5 LED Light Source (Zeiss). For electrical stimulation, glass stimulating electrodes were placed in the auditory nerve root and 20µs current pulses were generated with a DS3 current stimulator (Digitimer).

Analysis and Statistical Tests

Cell counts and habenula measurements were performed in ImageJ/FIJI software (National Institutes of Health). Electrophysiology data were analyzed using custom scripts and NeuroMatic analysis routines[118] in Igor Pro (Wavemetrics).

For data with equal variance (Levene's test), one-way ANOVAs with Tukey's HSD post hoc test were used where appropriate to determine statistical significance. For data with non-homogenous variances, one-way ANOVAs with a Welch F test were used with a Tukey's HSD post hoc test. Errors

and error bars report standard deviation (SD) or standard error of the mean (SEM) as noted in figure legends and throughout the text.

Computational Modelling

Computer simulations were performed using the NEURON 8.2 simulation environment[119], with an integration time constant of 25μs. The morphology of the octopus neuron was obtained from McGinley et al., 2012. The active and passive properties of the model were optimized to match the experimental recordings. We set the passive parameters as follows: internal or axial resistance (R_i or R_a) to 150Ω.cm, membrane resistance (R_m) to 5KΩ.cm^2, capacitance (C_m) to 0.9μF/Cm^2 and resting membrane potential (V_m) to -65mV. We included the following ion-channel conductances in our morphologically realistic octopus neuron model: Fast Na^+ ($\bar{g}_{NA}$), low-voltage activated K^+ ($\bar{g}_{KLT}$), high threshold K^+ ($\bar{g}_{KHT}$), fast transient K^+ ($\bar{g}_{KA}$), hyperpolarization-activated cyclic nucleotide-gated HCN ($\bar{g}_h$), leak K^+ ($\bar{g}_{leak}$). The kinetics of all the active ion-channel conductances were obtained from Manis and Campagnola, 2018 and the maximal conductance was optimized to match experimental data. We introduced a scaling factor (scl) to scale the maximal conductance to match the sag and input resistance of the experimental recordings (**Supp. Fig. 4**). Reversal potentials for HCN, Na^+ and K^+ respectively were (in mV), E_h= -38, E_{Na}= 50 and E_K= -70. Excitatory AMPA synaptic conductance and Inhibitory glycine synaptic conductance were introduced in the proximal and distal dendrites to test the impact of dendritic inhibition on the EPSP height and peak time. The rise and decay time of AMPA and glycine conductance were set to 0.3ms and 3ms respectively, to mimic the fast synaptic transients observed in octopus cells. The reversal potential of AMPA and glycine conductance was set to 0 and -80mV respectively.

	Experimental Genotype	*Abbreviation*	*Description*
Fig. 1B	*Glyt2*$^{Cre/+}$; Ai34$^{tg/+}$	*Glyt2*-syp/tdT	syp/tdT in *Glyt2* inhibitory neurons
Fig. 1C	*Glyt2*$^{Cre/+}$; Ai34$^{tg/+}$; *Thy1*$^{tg/+}$	*Glyt2*-syp/tdT; *Thy1*	syp/tdT in *Glyt2* inhibitory neurons; YFP octopus cells
Fig. 1D; 1F-G, black	*Foxg1*$^{Cre/+}$; Ai34$^{tg/+}$; *Thy1*$^{tg/+}$	*Foxg1*-syp/tdT; *Thy1*	syp/tdT in *Foxg1* SGNs; YFP octopus cells
Fig. 1E; 1F-G, green	*Glyt2*$^{Cre/+}$; Ai34$^{tg/+}$; *Thy1*$^{tg/+}$	*Glyt2*-syp/tdT; *Thy1*	syp/tdT in *Glyt2* inhibitory neurons; YFP octopus cells
Fig. 2B	*Ntng1*$^{Cre/+}$; Ai14$^{tg/+}$; *Foxg1*$^{Flp/+}$; RCE:FRT$^{tg/+}$	*Ntng1*-tdT; *Foxg1*-EYFP	tdT in *Ntng1* Ib/c SGNs; EYFP in all SGNs
Fig. 2C-E	*Ntng1*$^{Cre/+}$; Ai34$^{tg/+}$; *Thy1*$^{tg/+}$	*Ntng1*-syp/tdT; *Thy1*	syp/tdT in *Ntng1* Ib/c SGNs; YFP octopus cells
Fig. 3A-C, black	*Foxg1*$^{Cre/+}$; Ai32$^{tg/+}$	*Foxg1*-ChR2	ChR2 in *Foxg1* SGNs
Fig. 3A-C, magenta	*Ntng1*$^{Cre/+}$; Ai32$^{tg/+}$	*Ntng1*-ChR2	ChR2 in *Ntng1* Ib/c SGNs
Fig. 4A-C	*Glyt2*$^{Cre/+}$; Ai32$^{tg/+}$	*Glyt2*-ChR2	ChR2 in *Glyt2* inhibitory neurons
Fig. 5F-H	*Glyt2*$^{Cre/+}$; Ai32$^{tg/+}$	*Glyt2*-ChR2	ChR2 in *Glyt2* inhibitory neurons
Fig. S1A-D	*Ntng1*$^{Cre/+}$; Ai14$^{tg/+}$; *Foxg1*$^{Flp/+}$; RCE:FRT$^{tg/+}$	*Ntng1*-tdT; *Foxg1*-EYFP	tdT in *Ntng1* Ib/c SGNs; EYFP in all SGNs
Fig. S1E	*Ntng1*$^{Cre/+}$; Ai14$^{tg/+}$	*Ntng1*-tdT	tdT in *Ntng1* Ib/c SGNs and other neurons
Fig. S1F	*Ntng1*$^{Cre/+}$; Ai34$^{tg/+}$	*Ntng1*-syp/tdT	syp/tdT in *Ntng1* Ib/c SGNs
Fig. S2A-F	*Myo15*$^{iCre/+}$; Ai14$^{tg/+}$; *Foxg1*$^{Flp/+}$; RCE:FRT$^{tg/+}$	*Myo15*-tdT; *Foxg1*-EYFP	tdT in *Myo15* Ic SGNs; EYFP in all SGNs
Fig. S2G-I	*Myo15*$^{iCre/+}$; Ai34$^{tg/+}$; *Thy1*$^{tg/+}$	*Myo15*-syp/tdT; *Thy1*	syp/tdT in *Myo15* Ic SGNs; YFP octopus cells

Supplementary Table 1.

Summary and description of experimental genotypes presented in figures.

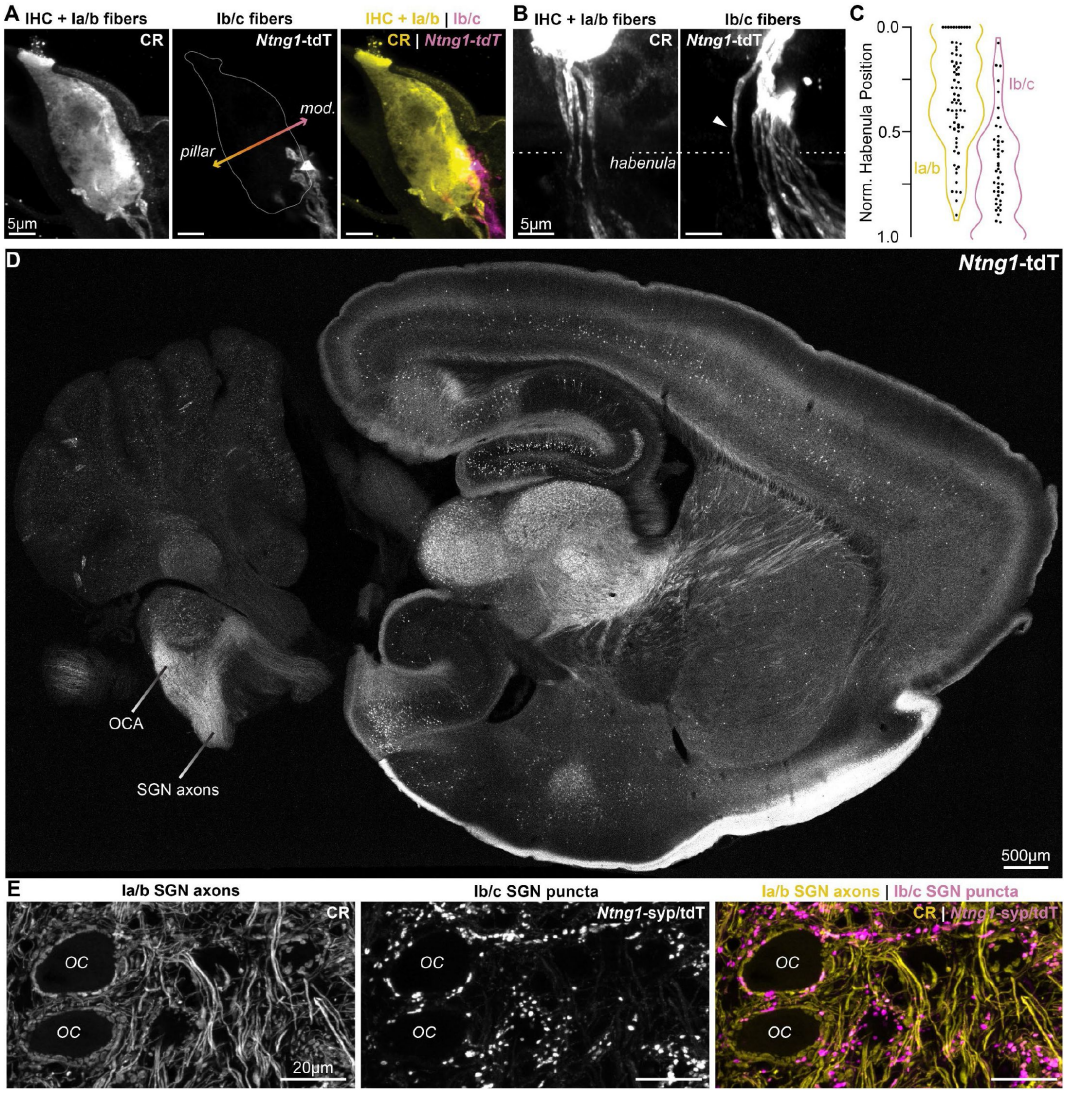

Supplementary Figure 1.

Ntng1^{Cre} has high specificity for Ib/c SGNs.

(A) Calretinin immunopositive (CR+) Ia/b fibers (CR, yellow) preferentially innervate the pillar side of inner hair cells (IHCs). Ib/c fibers with *Ntng1*^{Cre}-mediated expression of tdTomato (*Ntng1*-tdT, magenta) preferentially innervate the modiolar side of IHCs. IHCs also immunolabel for CR. **(B)** CR+ Ia/b fibers (yellow) pass through the pillar side of the habenula while *Ntng1*-tdT+ Ib/c fibers (magenta) pass through the modiolar side. Arrowhead highlights a *Ntng1*-tdT fiber passing through the pillar side of the habenula but ultimately terminating on the modiolar side of the IHC. **(C)** Normalized position of CR+ Ia/b (yellow) and *Ntng1*-tdT+ Ib/c (magenta) fibers along the pillar to modiolar axis of the habenula (*n* = 124 fibers; 5 mice). **(D)** In the central nervous system, *Ntng1*-tdT is present throughout the brain, but is restricted to SGN axons in the ventral cochlear nucleus where the octopus cell area (OCA) is found. **(E)** In the OCA, CR immunolabel is present in Ia/b SGN axons and puncta. As in the ganglion, CR co-labels with some Ib/c puncta (*Ntng1*-syp/tdT).

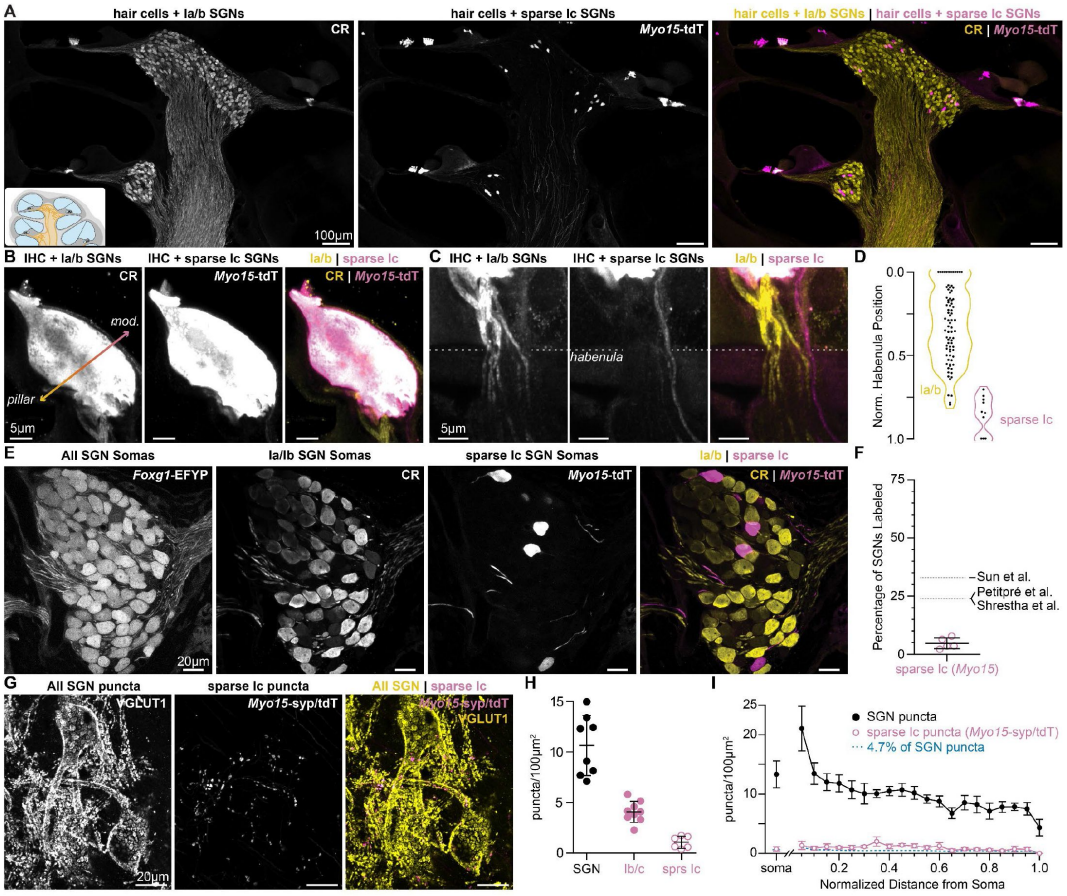

Supplementary Figure 2.

Myo15^{iCre} sparsely labels Ic SGNs.

(A) Cochlear sections with calretinin (CR) immunolabeling of hair cells and type Ia/b SGNs and *Myo15*^{iCre}-mediated expression of tdTomato (*Myo15*-tdT) in hair cells and some type Ic SGNs. **(B)** CR+ Ia/b fibers (yellow) preferentially innervate the pillar side of IHCs. Sparse Ic fibers with *Myo15*-tdT (magenta) preferentially innervate the modiolar side of IHCs. IHCs label with both tdT and CR. **(C)** CR+ Ia/b fibers (yellow) pass through the pillar side of the habenula while sparsely labeled *Myo15*-tdT+ Ic fibers (magenta) pass through the modiolar side. **(D)** Normalized position of CR+ Ia/b (yellow) and *Myo15*-tdT+ Ic (magenta) fibers along the pillar to modiolar axis of the habenula (*n* = 90 fibers; 4 mice). **(E)** 65µm cochlear section containing SGN somas. SGNs have variable levels of calretinin (CR) immunolabeling corresponding to the three molecular subtypes. Ia/b SGN somas label with high and medium levels of CR, respectively. Ic somas label with very low levels of CR. *Myo15*-tdT is sparsely found in Ic SGNs. All SGN somas are labeled with *Foxg1*^{Flp}-mediated expression of EYFP (*Foxg1*-EYFP). **(F)** tdT+CR-SGNs make up 4.7 ± 2.3% of the SGN population (*n* = 2150 neurons, 5 mice), indicating sparse reporter expression. Data are presented as mean ± SD; individual data points signify percent coverage per animal. Dotted lines are estimated percentages for type Ic SGNs from 1: Petitpré et al., 2018, 2: Shrestha et al., 2018, and 3: Sun et al., 2018. **(G)** In the OCA, VGlut1 immunolabel neatly tiles around octopus cells with sparse *Myo15*-syp/tdT puncta. **(H)** Density of all SGNs (black: data from **Fig. 1D**), Ib/c SGNs (magenta: data from **Fig. 2D**), and sparse Ic inputs (open magenta circles: 1.1 ± 0.6, *n* = 6 cells, 3 mice). Data are presented as mean ± SD. Markers represent the total puncta density computed per reconstructed octopus cell. **(I)** Puncta density per 100µm^2 of soma surface area (all SGN, black: data from **Fig. 1E**; sparse I/c inputs, magenta open circles: 0.7 ± 0.4, *n* = 6 cells, 3 mice) and density along the length of the dendritic tree, relative to the soma. Data are presented as mean ± SEM.

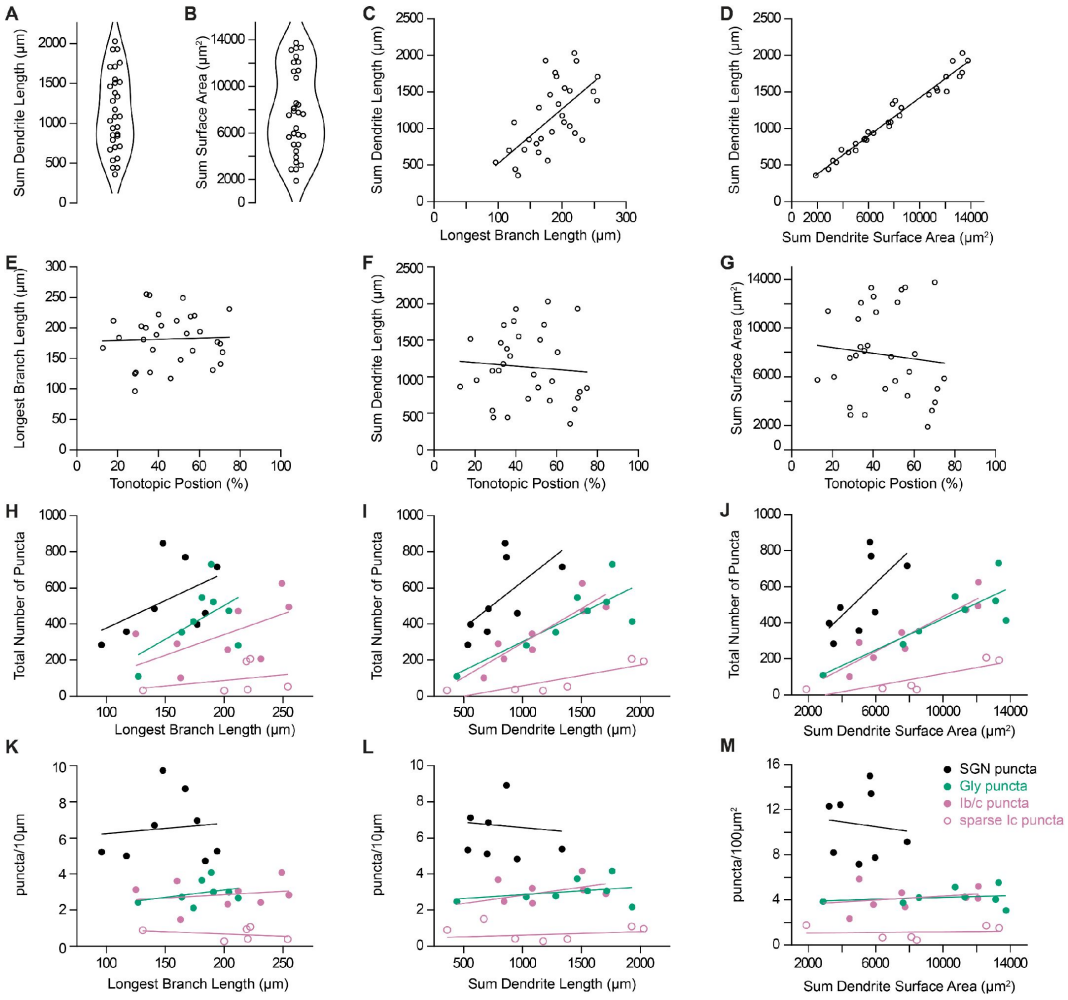

Supplementary Figure 3.

Dendritic and synaptic reconstructions of octopus cells.

(A) Total length of reconstructed dendritic arbors for 31 octopus cells. **(B)** Total surface area of reconstructed dendritic arbors for 31 octopus cells. **(C)** Octopus cell reconstructions were normalized to the longest reconstructed dendrite. Total length of reconstructed dendrites correlated with the longest branch per neuron. **(D)** Total length of reconstructed dendrites correlated with total dendritic surface area. **(E-G)** Longest branch length, total dendrite length, and total surface area compared to estimated position of the octopus cell soma in the tonotopic organization of the OCA. **(H-J)** Total number of reconstructed SGN puncta (*Foxg1*-syp/tdT, black), inhibitory puncta (*Glyt2*-syp/tdT, green), Ib/c SGN puncta (*Ntng1*-syp/tdT, magenta), and sparse Ic SGN puncta (*Myo15*-syp/tdT, open magenta circles) compared to the longest branch length, total dendrite length, and total dendrite surface area. **(K-M)** Density of reconstructed SGN puncta (*Foxg1*-syp/tdT, black), inhibitory puncta (*Glyt2*-syp/tdT, green), Ib/c SGN puncta (*Ntng1*-syp/tdT, magenta), and sparse Ic SGN puncta (*Myo15*-syp/tdT, open magenta circles) compared to longest branch length, total dendrite length, and total dendrite surface area.

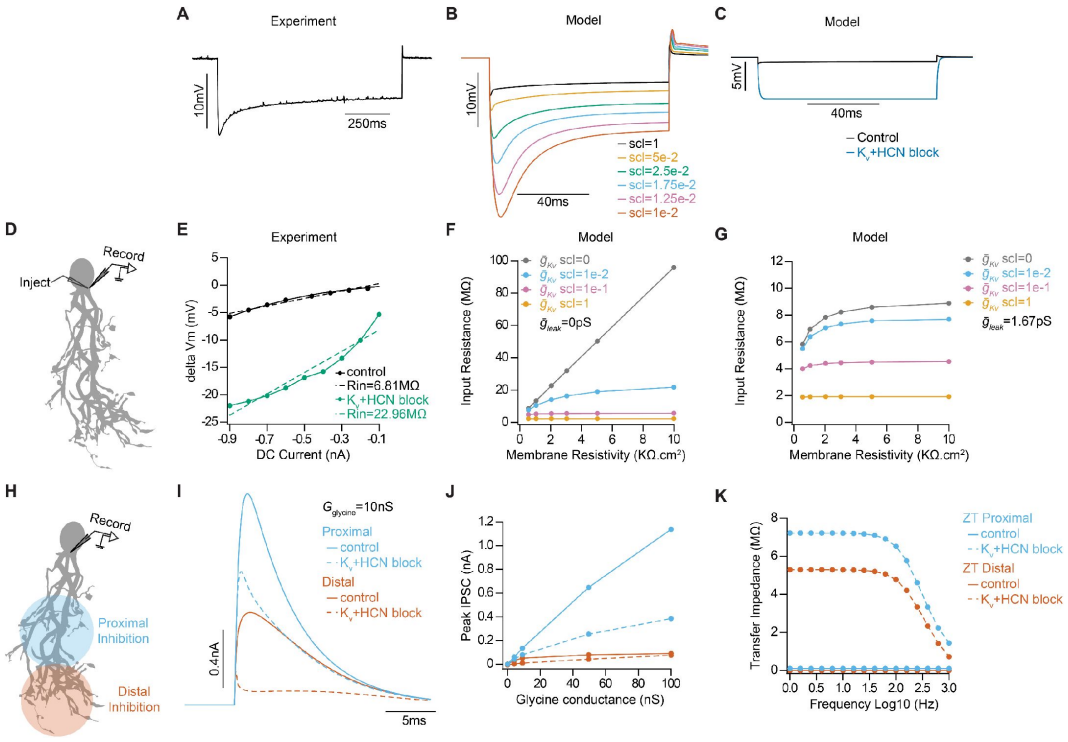

Supplementary Figure 4.

Optimizing active and passive properties of an octopus cell model.

(A) Subthreshold somatic voltage response to a hyperpolarizing current injection in an *in vitro* whole-cell current clamp recording of an octopus cell. **(B)** Somatic voltage responses from a morphologically realistic octopus cell model for various scaling factors of maximal conductances of active ion-channels. **(C)** Comparison of somatic hyperpolarizations in a model reproducing experimental data during control (black) and K_V and HCN block conditions (blue). **(D)** Illustration of injection and recording locations for panels *E-G* in a morphologically realistic octopus cell model. **(E)** IV curves (change in somatic membrane potential as function of current injection magnitude) from a representative experimental octopus cell. Dotted lines plot linear fits of the experimental data. Rin dotted line is the slope of the fit. **(F-G)** Impact of leak conductance ($\bar{g}_{leak}$) and scaling factor (scl) on passive properties of the model. Input resistance of the octopus neuron model as a function of membrane resistivity (Rm) with $\bar{g}_{leak}$=0 *(F)* and $\bar{g}_{leak}$=1.67 pS *(g)* for various scaling factor values indicated in different colors. **(H)** Illustration of injection and recording locations for panels *I-K* in a morphologically realistic octopus cell model. **(I)** Inhibitory post synaptic currents (IPSCs) recorded from glycinergic synapses in proximal (blue) and distal (orange) stimulation during control (solid) and K_V and HCN block conditions (dotted). **(J)** Peak IPSC magnitude as function of glycine conductance in proximal (blue) and distal (orange) stimulation during control (solid) and K_V and HCN block conditions (dotted). **(K)** Transfer impedance as function of frequency from proximal dendrites to soma (blue) and distal dendrites to soma (orange) during control (solid) and K_V and HCN block conditions (dotted).

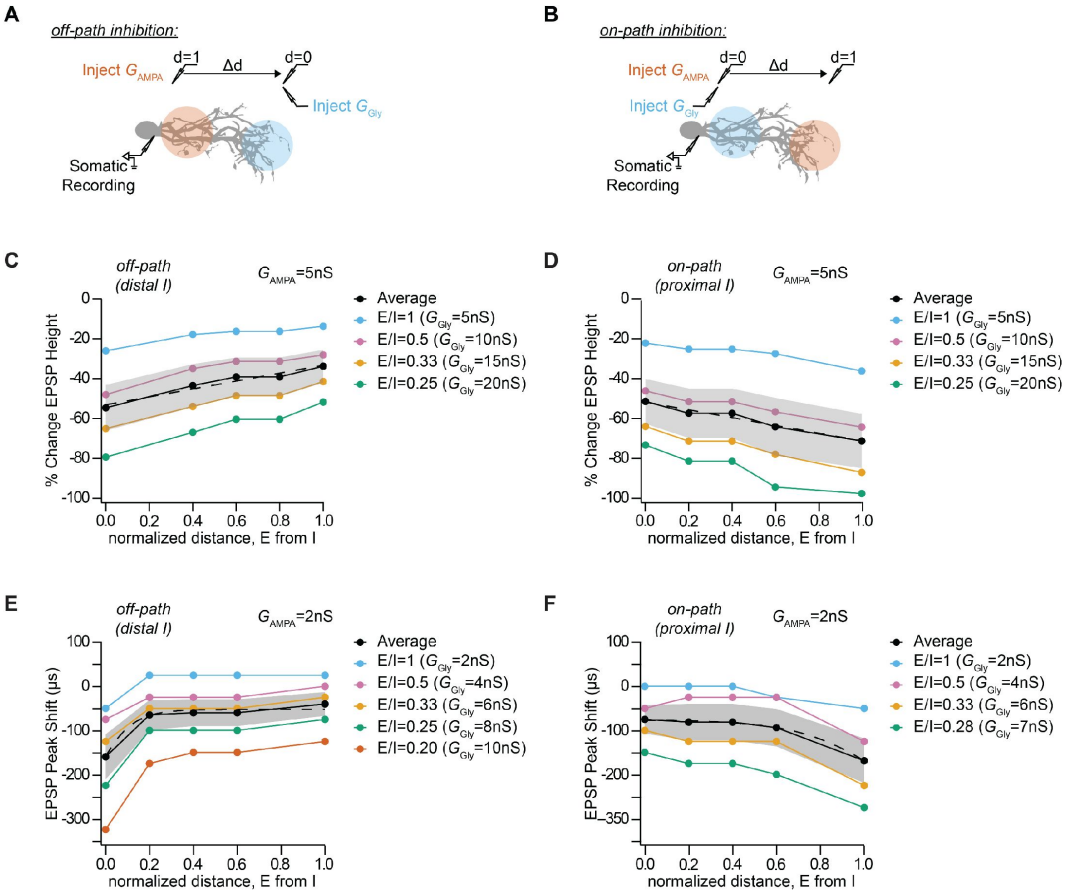

Supplementary Figure 5.

Impact of inhibitory synaptic location and distance between excitatory and inhibitory synapse on somatic EPSP amplitude and timing.

(A-B) Illustration of injection and recording locations for off-path *(A)* and on-path *(B)* inhibition paradigms and the normalized relative distance (d) between excitatory synapses. The impact of on-path and off-path inhibition in the dendrites is primarily determined by the local potential change by EPSP and the attenuation or the length constant (λ) of the IPSP towards the excitatory synaptic location. The exponential decay of membrane voltage is asymmetric, with lower λ for the open end and higher λ for sealed end propagation. Distal parts of the dendrites have higher local input resistance and lower attenuation of IPSP due to the sealed end. **(C-D)** Percentage change in somatic EPSP height with dendritic glycinergic inhibition as function of normalized distance between excitatory and inhibitory synapses in off-path *(C)* and on-path *(D)* inhibition for various E/I ratio with excitatory AMPA conductance (G_{AMPA}) set at 5nS. Average shown in black with SEM in shaded region. **(E-F)** Somatic EPSP peak time shift with dendritic glycinergic inhibition as function of normalized distance between excitatory and inhibitory synapses in off-path *(E)* and on-path *(F)* inhibition for various E/I ratio with excitatory AMPA conductance (G_{AMPA}) set at 2nS. Average shown in black with SEM in shaded region.

References

1. Shamma S.A., Elhilali M., Micheyl C. (2011) **Temporal coherence and attention in auditory scene analysis** *Trends Neurosci* **34**:114–123 https://doi.org/10.1016/j.tins.2010.11.002

2. Pressnitzer D., Suied C., Shamma S. (2011) **Auditory scene analysis: The sweet music of ambiguity** *Front. Hum. Neurosci* **5**

3. Osen K.K. (1969) **The intrinsic organization of the cochlear nuclei in the cat** *Acta Otolaryngol. (Stockh* **67**:352–359 https://doi.org/10.3109/00016486909125462

4. Osen K.K. (1969) **Cytoarchitecture of the cochlear nuclei in the cat** *J. Comp. Neurol* **136**:453–483 https://doi.org/10.1002/cne.901360407

5. Godfrey D.A., Kiang N.Y.S., Norris B.E. (1975) **Single unit activity in the posteroventral cochlear nucleus of the cat** *J. Comp. Neurol* **162**:247–268 https://doi.org/10.1002/cne.901620206

6. Recio-Spinoso A., Rhode W.S. (2020) **Information Processing by Onset Neurons in the Cat Auditory Brainstem** *JARO - J. Assoc. Res. Otolaryngol* **21**:201–224 https://doi.org/10.1007/s10162-020-00757-0

7. Rhode W.S., Smith P.H., Oertel D. (1983) **Physiological response properties of cells labeled intracellularly with horseradish peroxidase in cat dorsal cochlear nucleus** *J. Comp. Neurol* **213**:426–447 https://doi.org/10.1002/cne.902130407

8. Ritz L.A., Brownell W.E. (1982) **Single unit analysis of the posteroventral cochlear nucleus of the decerebrate cat** *Neuroscience* **7**:1995–2010 https://doi.org/10.1016/0306-4522(82)90013-6

9. Bal R., Oertel D. (2000) **Hyperpolarization-activated, mixedcation current (I(h)) in octopus cells of the mammalian cochlear nucleus** *J. Neurophysiol* **84**:806–817 https://doi.org/10.1152/jn.2000.84.2.806

10. Bal R., Oertel D. (2001) **Potassium currents in octopus cells of the mammalian cochlear nucleus** *J. Neurophysiol* **86**:2299–2311 https://doi.org/10.1152/jn.2001.86.5.2299

11. Cao X.J., Oertel D. (2017) **Genetic perturbations suggest a role of the resting potential in regulating the expression of the ion channels of the KCNA and HCN families in octopus cells of the ventral cochlear nucleus** *Hear. Res* **345**:57–68 https://doi.org/10.1016/j.heares.2017.01.001

12. Golding N.L., Robertson D., Oertel D. (1995) **Recordings from slices indicate that octopus cells of the cochlear nucleus detect coincident firing of auditory nerve fibers with temporal precision** *J. Neurosci* **15**:3138–3153 https://doi.org/10.1523/jneurosci.15-04-03138.1995

13. Golding N.L., Ferragamo M.J., Oertel D. (1999) **Role of intrinsic conductances underlying responses to transients in octopus cells of the cochlear nucleus** *J. Neurosci* **19**:2897–2905 https://doi.org/10.1523/jneurosci.19-08-02897.1999

14. Golding N.L., Oertel D. (2012) **Synaptic integration in dendrites: Exceptional need for speed** *J. Physiol* **590**:5563–5569 https://doi.org/10.1113/jphysiol.2012.229328

15. Manis P.B., Marx S.O. (1991) **Outward currents in isolated ventral cochlear nucleus neurons** *J. Neurosci* **11**:2865–2880 https://doi.org/10.1523/jneurosci.11-09-02865.1991

16. Oertel D. (1983) **Synaptic responses and electrical properties of cells in brain slices of the mouse anteroventral cochlear nucleus** *J. Neurosci* **3**:2043–2053 https://doi.org/10.1523/jneurosci.03-10-02043.1983

17. McGinley M.J., Cuntz H., Remme M. W. H., Torben-Nielsen B. (2014) **Rapid Integration Across Tonotopy by Individual Auditory Brainstem Octopus Cells** *The Computing Dendrite, From Structure to Function* :223–243 https://doi.org/10.1007/978-1-4614-8094-5_14

18. McGinley M.J., Liberman M.C., Bal R., Oertel D. (2012) **Generating Synchrony from the Asynchronous: Compensation for Cochlear Traveling Wave Delays by the Dendrites of Individual Brainstem Neurons** *J. Neurosci* **32**:9301–9311 https://doi.org/10.1523/jneurosci.0272-12.2012

19. Lu H.W., Smith P.H., Joris P.X. (2018) **Submillisecond monaural coincidence detection by octopus cells** *Acta Acust. United Acust* **104**:852–855 https://doi.org/10.3813/AAA.919238

20. Smith P.H., Massie A., Joris P.X. (2005) **Acoustic stria: Anatomy of physiologically characterized cells and their axonal projection patterns** *J. Comp. Neurol* **482**:349–371 https://doi.org/10.1002/cne.20407

21. Smith P.H., Joris P.X., Banks M.I., Yin T.C.T., Merchán M. A., Juiz J. M., Godfrey D. A., Mugnaini E. (1993) **Responses of Cochlear Nucleus Cells and Projections of their Axons** *In The Mammalian Cochlear Nuclei: Organization and Function NATO ASI series* :349–360 https://doi.org/10.1007/978-1-4615-2932-3_27

22. Cai Y., McGee J., Walsh E.J. (2000) **Contributions of Ion Conductances to the Onset Responses of Octopus Cells in the Ventral Cochlear Nucleus: Simulation Results** *J. Neurophysiol* **83**:301–314 https://doi.org/10.1152/jn.2000.83.1.301

23. Cai Y., Walsh E.J., McGee J. (1997) **Mechanisms of Onset Responses in Octopus Cells of the Cochlear Nucleus: Implications of a Model** *J. Neurophysiol* **78**:872–883 https://doi.org/10.1152/jn.1997.78.2.872

24. Kipke D.R., Levy K.L. (1997) **Sensitivity of the cochlear nucleus octopus cell to synaptic and membrane properties: A modeling study** *J. Acoust. Soc. Am* **102**:403–412 https://doi.org/10.1121/1.419762

25. Levy K.L., Kipke D.R. (1998) **Mechanisms of the cochlear nucleus octopus cell's onset response: Synaptic effectiveness and threshold** *J. Acoust. Soc. Am* **103**:1940–1950 https://doi.org/10.1121/1.421346

26. Levy K.L., Kipke D.R. (1997) **A computational model of the cochlear nucleus octopus cell** *J. Acoust. Soc. Am* **102**:391–402 https://doi.org/10.1121/1.419761

27. Rebhan M., Leibold C. (2021) **A phenomenological spiking model for octopus cells in the posterior–ventral cochlear nucleus** *Biol. Cybern* **115**:331–341 https://doi.org/10.1007/s00422-021-00881-x

28. Spencer M., Grayden D., Bruce I., Meffin H., Burkitt A. (2012) **An investigation of dendritic delay in octopus cells of the mammalian cochlear nucleus** *Front. Comput. Neurosci* **6** https://doi.org/10.3389/fncom.2012.00083

29. Lu H.-W., Smith P.H., Joris P.X. (2022) **Mammalian octopus cells are direction selective to frequency sweeps by excitatory synaptic sequence detection** *Proc. Natl. Acad. Sci* **119** https://doi.org/10.1073/pnas.2203748119

30. Gómez-Nieto R., Rubio M.E. (2009) **A bushy cell network in the rat ventral cochlear nucleus** *J. Comp. Neurol* **516**:241–263 https://doi.org/10.1002/cne.22139

31. Zhou J., Nannapaneni N., Shore S. (2007) **Vessicular glutamate transporters 1 and 2 are differentially associated with auditory nerve and spinal trigeminal inputs to the cochlear nucleus** *J. Comp. Neurol* **500**:777–787 https://doi.org/10.1002/cne.21208

32. Liberman M.C. (1991) **Central projections of auditory-nerve fibers of differing spontaneous rate** *I. Anteroventral cochlear nucleus. J. Comp. Neurol* **313**:240–258 https://doi.org/10.1002/cne.903130205

33. Liberman M.C. (1993) **Central projections of auditory nerve fibers of differing spontaneous rate, II: Posteroventral and dorsal cochlear nuclei** *J. Comp. Neurol* **327**:17–36 https://doi.org/10.1002/cne.903270103

34. Rouiller E.M., Cronin-Schreiber R., Fekete D.M., Ryugo D.K. (1986) **The central projections of intracellularly labeled auditory nerve fibers in cats: an analysis of terminal morphology** *J. Comp. Neurol* **249**:261–278 https://doi.org/10.1002/cne.902490210

35. Rouiller E.M., Ryugo D.K. (1984) **Intracellular marking of physiologically characterized cells in the ventral cochlear nucleus of the cat** *J. Comp. Neurol* **225**:167–186 https://doi.org/10.1002/cne.902250203

36. Tsuji J., Liberman M.C. (1997) **Intracellular labeling of auditory nerve fibers in guinea pig: central and peripheral projections** *J. Comp. Neurol* **381**:188–202

37. Liberman L.D., Wang H., Liberman M.C. (2011) **Opposing Gradients of Ribbon Size and AMPA Receptor Expression Underlie Sensitivity Differences among Cochlear-Nerve/Hair-Cell Synapses** *J. Neurosci* **31**:801–808 https://doi.org/10.1523/JNEUROSCI.3389-10.2011

38. Liberman M.C. (1978) **Auditory-nerve response from cats raised in a low-noise chamber** *J. Acoust. Soc. Am* **63**:442–455 https://doi.org/10.1121/1.381736

39. Liberman M.C. (1982) **Single-neuron labeling in the cat auditory nerve** *Science* **216**:1239–1241 https://doi.org/10.1126/science.7079757

40. Petitpré C. *et al.* (2018) **Neuronal heterogeneity and stereotyped connectivity in the auditory afferent system** *Nat. Commun* **9** https://doi.org/10.1038/s41467-018-06033-3

41. Shrestha B.R., Chia C., Wu L., Kujawa S.G., Liberman M.C., Goodrich L.V. (2018) **Sensory Neuron Diversity in the Inner Ear Is Shaped by Activity** *Cell* **174**:1229–1246 https://doi.org/10.1016/j.cell.2018.07.007

42. Siebald C., Vincent P.F.Y., Bottom R.T., Sun S., Reijntjes D.O.J., Manca M., Glowatzki E., Müller U. (2023) **Molecular signatures define subtypes of auditory afferents with distinct peripheral projection patterns and physiological properties** *Proc. Natl. Acad. Sci. U. S. A* **120** https://doi.org/10.1073/pnas.2217033120

43. Sun S., Babola T., Pregernig G., So K.S., Nguyen M., Su S.-S.M., Palermo A.T., Bergles D.E., Burns J.C., Müller U. (2018) **Hair Cell Mechanotransduction Regulates Spontaneous Activity and Spiral Ganglion Subtype Specification in the Auditory System** *Cell* **174**:1247–1263 https://doi.org/10.1016/j.cell.2018.07.008

44. Bolding K.A., Nagappan S., Han B.-X., Wang F., Franks K.M. (2020) **Recurrent circuitry is required to stabilize piriform cortex odor representations across brain states** *eLife* **9** https://doi.org/10.7554/eLife.53125

45. Muniak M.A., Rivas A., Montey K.L., May B.J., Francis H.W., Ryugo D.K. (2013) **3D model of frequency representation in the cochlear nucleus of the CBA/J mouse** *J. Comp. Neurol* **521**:1510–1532 https://doi.org/10.1002/cne.23238

46. Zhang Y.-P., Oertner T.G. (2007) **Optical induction of synaptic plasticity using a light-sensitive channel** *Nat. Methods* **4**:139–141 https://doi.org/10.1038/nmeth988

47. Jackman S.L., Beneduce B.M., Drew I.R., Regehr W.G. (2014) **Achieving High-Frequency Optical Control of Synaptic Transmission** *J. Neurosci* **34**:7704–7714 https://doi.org/10.1523/jneurosci.4694-13.2014

48. Oertel D., Bal R., Gardner S. (2000) **Detection of synchrony in the activity of auditory nerve fibers by octopus cells of the mammalian cochlear nucleus** *Proc. Of* **97**:11773–11779 https://doi.org/10.1073/pnas.97.22.11773

49. Cao X.J., Oertel D. (2010) **Auditory nerve fibers excite targets through synapses that vary in convergence, strength, and short-term plasticity** *J. Neurophysiol* **104**:2308–2320 https://doi.org/10.1152/jn.00451.2010

50. Cao X.-J., McGinley M.J., Oertel D. (2008) **Connections and synaptic function in the posteroventral cochlear nucleus of deaf jerker mice** *J. Comp. Neurol* **510**:297–308 https://doi.org/10.1002/cne.21788

51. Bal R., Baydas G., Naziroglu M. (2009) **Electrophysiological properties of ventral cochlear nucleus neurons of the dog** *Hear. Res* **256**:93–103 https://doi.org/10.1016/j.heares.2009.07.004

52. Oertel D., Wu S.H., Garb M.W., Dizack C. (1990) **Morphology and physiology of cells in slice preparations of the posteroventral cochlear nucleus of mice** *J. Comp. Neurol* **295**:136–154 https://doi.org/10.1002/cne.902950112

53. Lynch J.W., Rajendra S., Barry P.H., Schofield P.R. (1995) **Mutations Affecting the Glycine Receptor Agonist Transduction Mechanism Convert the Competitive Antagonist, Picrotoxin, into an Allosteric Potentiator** *J. Biol. Chem* **270**:13799–13806 https://doi.org/10.1074/jbc.270.23.13799

54. Pribilla I., Takagi T., Langosch D., Bormann J., Betz H. (1992) **The atypical M2 segment of the beta subunit confers picrotoxinin resistance to inhibitory glycine receptor channels** *EMBO J* **11**:4305–4311 https://doi.org/10.1002/j.1460-2075.1992.tb05529.x

55. Wang D.-S., Mangin J.-M., Moonen G., Rigo J.-M., Legendre P. (2006) **Mechanisms for Picrotoxin Block of α2 Homomeric Glycine Receptors** *J. Biol. Chem* **281**:3841–3855 https://doi.org/10.1074/jbc.M511022200

56. Hruskova B., Trojanova J., Kulik A., Kralikova M., Pysanenko K., Bures Z., Syka J., Trussell L.O., Turecek R. (2012) **Differential Distribution of Glycine Receptor Subtypes at the Rat Calyx of Held Synapse** *J. Neurosci* **32**:17012–17024 https://doi.org/10.1523/JNEUROSCI.1547-12.2012

57. Zhang X.-B., Sun G.-C., Liu L.-Y., Yu F., Xu T.-L. (2008) **Alpha2 subunit specificity of cyclothiazide inhibition on glycine receptors** *Mol. Pharmacol* **73**:1195–1202 https://doi.org/10.1124/mol.107.042655

58. Dutertre S., Becker C.-M., Betz H. (2012) **Inhibitory Glycine Receptors: An Update *** *J. Biol. Chem* **287**:40216–40223 https://doi.org/10.1074/jbc.R112.408229

59. Lynch J.W. (2009) **Native glycine receptor subtypes and their physiological roles** *Neuropharmacology* **56**:303–309 https://doi.org/10.1016/j.neuropharm.2008.07.034

60. Veruki M.L., Gill S.B., Hartveit E. (2007) **Spontaneous IPSCs and glycine receptors with slow kinetics in wide-field amacrine cells in the mature rat retina** *J. Physiol* **581**:203–219 https://doi.org/10.1113/jphysiol.2006.127316

61. Manis P.B., Campagnola L. (2018) **A biophysical modelling platform of the cochlear nucleus and other auditory circuits: From channels to networks** *Hear. Res* **360**:76–91 https://doi.org/10.1016/j.heares.2017.12.017

62. Mathie A., Wooltorton J.R.A., Watkins C.S. (1998) **Voltage-activated potassium channels in mammalian neurons and their block by novel pharmacological agents** *Gen. Pharmacol. Vasc. Syst* **30**:13–24 https://doi.org/10.1016/S0306-3623(97)00034-7

63. Koch C., Poggio T., Torre V. (1983) **Nonlinear interactions in a dendritic tree: localization, timing, and role in information processing** *Proc. Natl. Acad. Sci. U. S. A* **80**:2799–2802

64. Moser T., Karagulyan N., Neef J., Jaime Tobón L.M. (2023) **Diversity matters — extending sound intensity coding by inner hair cells via heterogeneous synapses** *EMBO J* **42** https://doi.org/10.15252/embj.2023114587

65. Costalupes J.A., Young E.D., Gibson D.J. (1984) **Effects of continuous noise backgrounds on rate response of auditory nerve fibers in cat** *J. Neurophysiol* **51**:1326–1344 https://doi.org/10.1152/jn.1984.51.6.1326

66. Buran B.N., Strenzke N., Neef A., Gundelfinger E.D., Moser T., Liberman M.C. (2010) **Onset Coding Is Degraded in Auditory Nerve Fibers from Mutant Mice Lacking Synaptic Ribbons** *J. Neurosci* **30**:7587–7597 https://doi.org/10.1523/JNEUROSCI.0389-10.2010

67. Oliver D., Taberner A.M., Thurm H., Sausbier M., Arntz C., Ruth P., Fakler B., Liberman M.C. (2006) **The Role of BKCa Channels in Electrical Signal Encoding in the Mammalian Auditory Periphery** *J. Neurosci* **26**:6181–6189 https://doi.org/10.1523/JNEUROSCI.1047-06.2006

68. Bourien J., Tang Y., Batrel C., Huet A., Lenoir M., Ladrech S., Desmadryl G., Nouvian R., Puel J.-L., Wang J. (2014) **Contribution of auditory nerve fibers to compound action potential of the auditory nerve** *J. Neurophysiol* **112**:1025–1039 https://doi.org/10.1152/jn.00738.2013

69. McGinley M.J., Oertel D. (2006) **Rate thresholds determine the precision of temporal integration in principal cells of the ventral cochlear nucleus** *Hear. Res* **216**:52–63 https://doi.org/10.1016/j.heares.2006.02.006

70. Zhang C., Wang M., Lin S., Xie R. (2022) **Calretinin-Expressing Synapses Show Improved Synaptic Efficacy with Reduced Asynchronous Release during High-Rate Activity** *J. Neurosci* **42**:2729–2742 https://doi.org/10.1523/JNEUROSCI.1773-21.2022

71. Huet A., Batrel C., Tang Y., Desmadryl G., Wang J., Puel J.-L., Bourien J. (2016) **Sound coding in the auditory nerve of gerbils** *Hear. Res* **338**:32–39 https://doi.org/10.1016/j.heares.2016.05.006

72. Stasheff S.F., Masland R.H. (2002) **Functional Inhibition in Direction-Selective Retinal Ganglion Cells: Spatiotemporal Extent and Intralaminar Interactions** *J. Neurophysiol* **88**:1026–1039 https://doi.org/10.1152/jn.2002.88.2.1026

73. Ding H., Smith R.G., Poleg-Polsky A., Diamond J.S., Briggman K.L. (2016) **Species-specific wiring for direction selectivity in the mammalian retina** *Nature* **535**:105–110 https://doi.org/10.1038/nature18609

74. Bloss E.B., Cembrowski M.S., Karsh B., Colonell J., Fetter R.D., Spruston N. (2016) **Structured Dendritic Inhibition Supports Branch-Selective Integration in CA1 Pyramidal Cells** *Neuron* **89**:1016–1030 https://doi.org/10.1016/j.neuron.2016.01.029

75. Gidon A., Segev I. (2012) **Principles governing the operation of synaptic inhibition in dendrites** *Neuron* **75**:330–341 https://doi.org/10.1016/j.neuron.2012.05.015

76. Hao J., Wang X., Dan Y., Poo M., Zhang X. (2009) **An arithmetic rule for spatial summation of excitatory and inhibitory inputs in pyramidal neurons** *Proc. Natl. Acad. Sci. U. S. A* **106**:21906–21911 https://doi.org/10.1073/pnas.0912022106

77. Iascone D.M. *et al.* (2020) **Whole-Neuron Synaptic Mapping Reveals Spatially Precise Excitatory/Inhibitory Balance Limiting Dendritic and Somatic Spiking** *Neuron* **106**:566–578 https://doi.org/10.1016/j.neuron.2020.02.015

78. Jadi M., Polsky A., Schiller J., Mel B.W. (2012) **Location-Dependent Effects of Inhibition on Local Spiking in Pyramidal Neuron Dendrites** *PLOS Comput. Biol* **8** https://doi.org/10.1371/journal.pcbi.1002550

79. Lovett-Barron M., Turi G.F., Kaifosh P., Lee P.H., Bolze F., Sun X.-H., Nicoud J.-F., Zemelman B.V., Sternson S.M., Losonczy A. (2012) **Regulation of neuronal input transformations by tunable dendritic inhibition** *Nat. Neurosci* **15**:423–430 https://doi.org/10.1038/nn.3024

80. Juiz J.M., Helfert R.H., Bonneau J.M., Wenthold R.J., Altschuler R.A. (1996) **Three classes of inhibitory amino acid terminals in the cochlear nucleus of the guinea pig** *J. Comp. Neurol* **373**:11–26

81. Kemmer M., Vater M. (1997) **The distribution of GABA and glycine immunostaining in the cochlear nucleus of the mustached bat (Pteronotus parnellii)** *Cell Tissue Res* **287**:487–506 https://doi.org/10.1007/s004410050773

82. Kolston J., Osen K.K., Hackney C.M., Ottersen O.P., Storm-Mathisen J. (1992) **An atlas of glycine- and GABA-like immunoreactivity and colocalization in the cochlear nuclear complex of the guinea pig** *Anat. Embryol. (Berl* **186**:443–465

83. Moore J.K., Osen K.K., Storm-Mathisen J., Ottersen O.P. (1996) **gamma-Aminobutyric acid and glycine in the baboon cochlear nuclei: an immunocytochemical colocalization study with reference to interspecies differences in inhibitory systems** *J. Comp. Neurol* **369**:497–519

84. Adams J.C., Mugnaini E. (1987) **Patterns of glutamate decarboxylase immunostaining in the feline cochlear nuclear complex studied with silver enhancement and electron microscopy** *J. Comp. Neurol* **262**:375–401 https://doi.org/10.1002/cne.902620305

85. Friauf E., Hammerschmidt B., Kirsch J. (1997) **Development of adult-type inhibitory glycine receptors in the central auditory system of rats** *J. Comp. Neurol* **385**:117–134 https://doi.org/10.1002/(sici)1096-9861(19970818)385:1<117::aid-cne7>3.0.co;2-5

86. Sato K., Kuriyama H., Altschuler R.A. (2000) **Expression of glycine receptor subunit mRNAs in the rat cochlear nucleus** *Hear. Res* **144**:47–52 https://doi.org/10.1016/s0378-5955(00)00044-7

87. Schofield B.R., Cant N.B. (1996) **Origins and targets of commissural connections between the cochlear nuclei in guinea pigs** *J. Comp. Neurol* **375**:128–146

88. Thompson G.C., Cortez A.M., Lam D.M.K. (1985) **Localization of GABA immunoreactivity in the auditory brainstem of guinea pigs** *Brain Res* **339**:119–122 https://doi.org/10.1016/0006-8993(85)90628-6

89. Ngodup T., Romero G.E., Trussell L.O. (2020) **Identification of an inhibitory neuron subtype, the L-stellate cell of the cochlear nucleus** *eLife* **9** https://doi.org/10.7554/eLife.54350

90. Wickesberg R.E., Whitlon D., Oertel D. (1991) **Tuberculoventral Neurons Project to the Multipolar Cell Area But Not to the Octopus Cell Area of the Posteroventral Cochlear Nucleus** *Journal of Comparative Neurology* **313**:457–468 https://doi.org/10.1002/cne.903130306

91. Kane E.S. (1977) **Descending inputs to octopus cell area of the cat cochlear nucleus: An electron microscopic study** *J. Comp. Neurol* **173**:337–354 https://doi.org/10.1002/cne.901730209

92. Felix R.A., Gourévitch B., Gómez-Álvarez M., Leijon S.C.M., Saldaña E., Magnusson A.K. (2017) **Octopus Cells in the Posteroventral Cochlear Nucleus Provide the Main Excitatory Input to the Superior Paraolivary Nucleus** *Front. Neural Circuits* **11**

93. Friauf E., Ostwald J. (1988) **Divergent projections of physiologically characterized rat ventral cochlear nucleus neurons as shown by intra-axonal injection of horseradish peroxidase** *Exp. Brain Res* **73**:263–284 https://doi.org/10.1007/BF00248219

94. Schofield B.R. (1995) **Projections from the cochlear nucleus to the superior paraolivary nucleus in guinea pigs** *J. Comp. Neurol* **360**:135–149 https://doi.org/10.1002/cne.903600110

95. Thompson A.M., Thompson G.C. (1991) **Projections from the posteroventral cochlear nucleus to the superior olivary complex in guinea pig: Light and em observations with the PHA-L method** *J. Comp. Neurol* **311**:495–508 https://doi.org/10.1002/cne.903110405

96. Zook J.M., Casseday J.H. (1985) **Projections from the cochlear nuclei in the mustache bat, Pteronotus parnellii** *J. Comp. Neurol* **237**:307–324 https://doi.org/10.1002/cne.902370303

97. Adams J.C. (1997) **Projections from octopus cells of the posteroventral cochlear nucleus to the ventral nucleus of the lateral lemniscus in cat and human** *Audit. Neurosci* **3**:335–350

98. Berger C., Meyer E.M.M., Ammer J.J., Felmy F. (2014) **Large Somatic Synapses on Neurons in the Ventral Lateral Lemniscus Work in Pairs** *J. Neurosci* **34**:3237–3246 https://doi.org/10.1523/JNEUROSCI.3664-13.2014

99. Nayagam D.A.X., Clarey J.C., Paolini A.G. (2005) **Powerful, Onset Inhibition in the Ventral Nucleus of the Lateral Lemniscus** *J. Neurophysiol* **94**:1651–1654 https://doi.org/10.1152/jn.00167.2005

100. Schofield B.R., Cant N.B. (1997) **Ventral nucleus of the lateral lemniscus in guinea pigs: Cytoarchitecture and inputs from the cochlear nucleus** *J. Comp. Neurol* **379**:363–385

101. Vater M., Feng A.S. (1990) **Functional organization of ascending and descending connections of the cochlear nucleus of horseshoe bats** *J. Comp. Neurol* **292**:373–395 https://doi.org/10.1002/cne.902920305

102. Kawaguchi D., Sahara S., Zembrzycki A., O'Leary D.D.M. (2016) **Generation and analysis of an improved Foxg1-IRES-Cre driver mouse line** *Dev. Biol* **412**:139–147 https://doi.org/10.1016/j.ydbio.2016.02.011

103. Hatini V., Ye X., Balas G., Lai E. (1999) **Dynamics of placodal lineage development revealed by targeted transgene expression** *Dev. Dyn* **215**:332–343

104. Pauley S., Lai E., Fritzsch B. (2006) **Foxg1 Is Required for Morphogenesis and Histogenesis of the Mammalian Inner Ear** *Dev. Dyn. Off. Publ. Am. Assoc. Anat* **235**:2470–2482 https://doi.org/10.1002/dvdy.20839

105. Hanashima C., Shen L., Li S.C., Lai E. (2002) **Brain Factor-1 Controls the Proliferation and Differentiation of Neocortical Progenitor Cells through Independent Mechanisms** *J. Neurosci* **22**:6526–6536 https://doi.org/10.1523/JNEUROSCI.22-15-06526.2002

106. Tao W., Lai E. (1992) **Telencephalon-restricted expression of BF-1, a new member of the HNF-3/fork head gene family, in the developing rat brain** *Neuron* **8**:957–966 https://doi.org/10.1016/0896-6273(92)90210-5

107. Miyoshi G., Fishell G. (2012) **Dynamic FoxG1 expression coordinates the integration of multipolar pyramidal neuron precursors into the cortical plate** *Neuron* **74**:1045–1058 https://doi.org/10.1016/j.neuron.2012.04.025

108. Lakso M., Pichel J.G., Gorman J.R., Sauer B., Okamoto Y., Lee E., Alt F.W., Westphal H. (1996) **Efficient in vivo manipulation of mouse genomic sequences at the zygote stage** *Proc. Natl. Acad. Sci. U. S. A* **93**:5860–5865 https://doi.org/10.1073/pnas.93.12.5860

109. Kakizaki T., Sakagami H., Sakimura K., Yanagawa Y. (2017) **A glycine transporter 2-Cre knock-in mouse line for glycinergic neuron-specific gene manipulation** *IBRO Rep* **3**:9–16 https://doi.org/10.1016/j.ibror.2017.07.002

110. Feng G., Mellor R.H., Bernstein M., Keller-Peck C., Nguyen Q.T., Wallace M., Nerbonne J.M., Lichtman J.W., Sanes J.R. (2000) **Imaging Neuronal Subsets in Transgenic Mice Expressing Multiple Spectral Variants of GFP** *Neuron* **28**:41–51 https://doi.org/10.1016/S0896-6273(00)00084-2

111. Caberlotto E. *et al.* (2011) **Usher type 1G protein sans is a critical component of the tip-link complex, a structure controlling actin polymerization in stereocilia** *Proc. Natl. Acad. Sci. U. S. A* **108**:5825–5830 https://doi.org/10.1073/pnas.1017114108

112. Madisen L. *et al.* (2010) **A robust and high-throughput Cre reporting and characterization system for the whole mouse brain** *Nat. Neurosci* **13**:133–140 https://doi.org/10.1038/nn.2467

113. Sousa V.H., Miyoshi G., Hjerling-Leffler J., Karayannis T., Fishell G. (2009) **Characterization of Nkx6-2-derived neocortical interneuron lineages** *Cereb. Cortex N. Y. N 1991* **19**:i1–i10 https://doi.org/10.1093/cercor/bhp038

114. Madisen L. *et al.* (2012) **A toolbox of Cre-dependent optogenetic transgenic mice for light-induced activation and silencing** *Nat. Neurosci* **15**:793–802 https://doi.org/10.1038/nn.3078

115. Connelly C.J., Ryugo D.K., Muniak M.A. (2017) **The effect of progressive hearing loss on the morphology of endbulbs of Held and bushy cells** *Hear. Res* **343**:14–33 https://doi.org/10.1016/j.heares.2016.07.004

116. Matsumoto K. *et al.* (2019) **Advanced CUBIC tissue clearing for whole-organ cell profiling** *Nat. Protoc* **14**:3506–3537 https://doi.org/10.1038/s41596-019-0240-9

117. Susaki E.A., Tainaka K., Perrin D., Yukinaga H., Kuno A., Ueda H.R. (2015) **Advanced CUBIC protocols for whole-brain and whole-body clearing and imaging** *Nat. Protoc* **10**:1709–1727 https://doi.org/10.1038/nprot.2015.085

118. Rothman J.S., Silver R.A. (2018) **NeuroMatic: An Integrated Open-Source Software Toolkit for Acquisition, Analysis and Simulation of Electrophysiological Data** *Front. Neuroinformatics* **12** https://doi.org/10.3389/fninf.2018.00014

119. Hines M.L., Carnevale N.T. (1997) **The NEURON simulation environment** *Neural Comput* **9**:1179–1209 https://doi.org/10.1162/neco.1997.9.6.1179

Editors

Reviewing Editor
Tatyana Sharpee
Salk Institute for Biological Studies, La Jolla, United States of America

Senior Editor
Andrew King
University of Oxford, Oxford, United Kingdom

Reviewer #1 (Public Review):

Kreeger and colleagues have explored the balance of excitation and inhibition in the cochlear nucleus octopus cells of mice using morphological, electrophysiological, and computational methods. On the surface, the conclusion, that synaptic inhibition is present, does not seem like a leap. However, the octopus cells have been in the past portrayed as devoid of inhibition. This view was supported by the seeming lack of glycinergic fibers in the octopus cell area and the lack of apparent IPSPs. Here, Kreeger et al. used beautiful immunohistochemical and mouse genetic methods to quantify the inhibitory and excitatory boutons over the complete surface of individual octopus cells and further analysed the proportions of the different subtypes of spiral ganglion cell inputs. I think the analysis stands as one of the most complete descriptions of any neuron, leaving little doubt about the presence of glycinergic boutons.

Kreeger et al then examined inhibition physiologically, but here I felt that the study was incomplete. Specifically, no attempt was made to assess the actual, biological values of synaptic conductance for AMPAR and GlyR. Thus, we don't really know how potent the GlyR could be in mediating inhibition. Here are some numbered comments:

(1) "EPSPs" were evoked either optogenetically or with electrical stimulation. The resulting depolarizations are interpreted to be EPSPs. However previous studies from Oertel show that octopus cells have tiny spikes, and distinguishing them from EPSPs is tricky. No mention is made here about how or whether that was done. Thus, the analysis of EPSP amplitude is ambiguous.

(2) For this and later analysis, a voltage clamp of synaptic inputs would have been a simple alternative to avoid contaminating spikes or shunts by background or voltage-gated conductances. Yet only the current clamp was employed. I can understand that the authors might feel that the voltage clamp is 'flawed' because of the failure to clamp dendrites. But that may have been a good price to pay in this case. The authors should have at least justified their choice of method and detailed its caveats.

(3) The modeling raised several concerns. First, there is little presentation of assumptions, and of course, a model is entirely about its assumptions. For example, what excitatory conductance amplitudes were used? The same for inhibitory conductance? How were these values arrived at? The authors note that EPSGs and IPSGs had peaks at 0.3 and 3 ms. On what basis were these numbers obtained? The model's conclusions entirely depend on these values, and no measurements were made here that could have provided them. Parenthetical reference is made to Figure S5 where a range of values are tested, but with little explanation or justification.

(4) In experiments that combined E and I stimulation, what exactly were time timecourses of the conductance changes, and how 'synchronous' were they, given the different methods to evoke them? (had the authors done voltage clamp they would know the answers).

(5) Figure 4G is confusing to me. Its point, according to the text, is to show that changes in membrane properties induced by a block of Kv and HCN channels would not be expected to alter the amplitudes of EPSCs and IPSCs across the dendritic expanse. Now we are talking about currents (not shunting effects), and the presumption is that the blockers would alter the resting potential and thus the driving force for the currents. But what was the measured membrane potential change in the blockers? Surely that was documented. To me, the bigger concern (stated in the text) is whether the blockers altered exocytosis, and thus the increase in IPSP amplitude in blockers is due BOTH to loss of shunting and increase in presynaptic spike width. Added to this is that 4AP will reduce the spike threshold, thus allowing more ChR2-expressing axons to reach the threshold. Figure 4G does not address this point.

(6) Figure 5F is striking as the key piece of biological data that shows that inhibition does reduce the amplitude of "EPSPs" in octopus cells. Given the other uncertainties mentioned, I wondered if it makes sense as an example of shunting inhibition. Specifically, what are the relative synaptic conductances, and would you predict a 25% reduction given the actual (not modeled) values?

(7) Some of the supplemental figures, like 4 and 5, are hardly mentioned. Few will glean anything from them unless the authors direct attention to them and explain them better. In general, the readers would benefit from more complete explanations of what was done.

https://doi.org/10.7554/eLife.100492.1.sa1

Reviewer #2 (Public Review):

Summary:

Kreeger et.al provided mechanistic evidence for flexible coincidence detection of auditory nerve synaptic inputs by octopus cells in the mouse cochlear nucleus. The octopus cells are specialized neurons that can fire repetitively at very high rates (> 800 Hz in vivo), yield responses dominated by the onset of sound for simple stimuli, and integrate auditory nerve inputs over a wide frequency span. Previously, it was thought that octopus cells received little inhibitory input, and their integration of auditory input depended principally on temporally precise coincidence detection of excitatory auditory nerve inputs, coupled with a low input resistance established by high levels of expression of certain potassium channels and hyperpolarization-activated channels.

In this study, the authors used a combination of numerous genetic mouse models to characterize synaptic inputs and enable optogenetic stimulation of subsets of afferents, fluorescent microscopy, detailed reconstructions of the location of inhibitory synapses on the soma and dendrites of octopus cells, and computational modeling, to explore the importance of inhibitory inputs to the cells. They determined through assessment of excitatory and inhibitory synaptic densities that spiral ganglion neuron synapses are densest on the soma and proximal dendrite, while glycenergic inhibitory synaptic density is greater on the dendrites compared to the soma of octopus cells. Using different genetic lines, the authors further elucidated that the majority of excitatory synapses on the octopus cells are from type 1a spiral ganglion neurons, which have low response thresholds and high rates of spontaneous activity. In the second half of the paper, the authors employed electrophysiology to uncover the physiological response of octopus cells to excitatory and inhibitory inputs. Using a combination of pharmacological blockers in vitro cellular and computational modeling, the authors conclude that glycine in fact evokes IPSPs in octopus cells; these IPSPs are largely shunted by the high membrane conductance of the cells under normal conditions and thus were not clearly evident in prior studies. Pharmacological experiments point towards a specific glycine receptor subunit composition. Lastly, Kreeger et. al demonstrated with in vitro recordings and computational modeling that octopus cell inhibition modulates the amplitude and timing of dendritic spiral ganglion inputs to octopus cells, allowing for flexible coincidence detection.

Strengths:

The work combines a number of approaches and complementary observations to characterize the spatial patterns of excitatory and inhibitory synaptic input, and the type of auditory nerve input to the octopus cells. The combination of multiple mouse lines enables a better understanding of and helps to define, the pattern of synaptic convergence onto these cells. The electrophysiology provides excellent functional evidence for the presence of the inhibitory inputs, and the modeling helps to interpret the likely functional role of inhibition. The work is technically well done and adds an interesting dimension related to the processing of sound by these neurons. The paper is overall well written, the experimental tests are well-motivated and easy to follow. The discussion is reasonable and touches on both the potential implications of the work as well as some caveats.

Weaknesses:

While the conclusions presented by the authors are solid, a prominent question remains regarding the source of the glycinergic input onto octopus cells. In the discussion, the authors claim that there is no evidence for D-stellate, L-stellate, and tuberculoventral cell (all local inhibitory neurons of the ventral and dorsal cochlear nucleus) connections to octopus cells, and cite the relevant literature. An experimental approach will be necessary to properly rule out (or rule in) these cell types and others that may arise from other auditory brainstem

nuclei. Understanding which cells provide the inhibitory input will be an essential step in clarifying its roles in the processing of sound by octopus cells.

The authors showed that type 1a SGNs are the most abundant inputs to octopus cells via microscopy. However, in Figure 3 they compare optical stimulation of all classes of ANFs, then compare this against stimulation of type 1b/c ANFs. While a difference in the paired-pulse ratio (and therefore, likely release probability) can be inferred by the difference between Foxg1-ChR2 and Ntng1-ChR2, it would have been preferable to have specific data with selective stimulation of type 1a neurons.

https://doi.org/10.7554/eLife.100492.1.sa0